

Vertical observations of the atmospheric boundary layer structure over Beijing urban area during air pollution episodes

Linlin Wang^{1,2}, Junkai Liu^{1,5}, Zhiqiu Gao^{1*}, Yubin Li², Meng Huang², Sihui Fan², Xiaoye Zhang³, Yuanjian Yang^{2,6}, Shiguang Miao⁴, Han Zou¹, Yele Sun¹, Yong Chen¹, Ting Yang¹

¹State Key Laboratory of Atmospheric Boundary Layer Physics and Atmospheric Chemistry

(LAPC), Institute of Atmospheric Physics, Chinese Academy of Sciences, Beijing 100029, China

² Collaborative Innovation Centre on Forecast and Evaluation of Meteorological Disasters, School

of Atmospheric Physics, Nanjing University of Information Science and Technology, Nanjing,

210044, China

³ Chinese Academy of Meteorological Sciences, Beijing, 100081, China

⁴ Institute of Urban Meteorology, China Meteorological Administration, Beijing, 100081, China

⁵ University of Chinese Academy of Sciences, Beijing 100049, China

⁶ State Key Laboratory of Loess and Quaternary Geology, Institute of Earth Environment, Chinese

Academy of Sciences, Xi'an 710061, China

Abstract

We investigated the interactions between the air pollutants and the structure of urban boundary layer (UBL) over Beijing by using the data mainly obtained from the 325-m meteorological tower and a Doppler wind lidar during 1–4 December, 2016. Results showed that the pollution episodes in this period could be characterized by low surface pressure, high relative humidity, weak wind, and temperature inversion. Compared with a clean daytime episode that took place on 1 December, results also showed that the attenuation ratio of downward shortwave radiation was about 5%, 24%

*Corresponding author: Dr. Zhiqiu Gao, zgao@mail.iap.ac.cn

26 and 63% in afternoon hours [from 1200 to 1400 local standard time (LST)] on 2–4
27 December respectively, while for the net radiation (R_n) attenuation ratio at the 140-m
28 level of the 325-m tower was 3%, 27%, and 68%. The large reduction in R_n on 4
29 December was not only the result of the aerosols, but also clouds. Based on analysis
30 of the surface energy balance at the 140-m level, we found that the sensible heat flux
31 was remarkably diminished during daytimes on polluted days, and even negative after
32 sunrise (about 0720 LST) till 1400 LST on 4 December. We also found that heat
33 storage in the urban surface layer played an important role in the exchange of the
34 sensible heat flux. Owing to the advantages of the wind lidar having superior spatial
35 and temporal resolution, the vertical velocity variance could capture the evolution of
36 the UBL well. It clearly showed that vertical mixing was negatively related to the
37 concentrating of pollutants, and that vertical mixing would also be weakened by a
38 certain quantity of pollutants, and then in turn worsened the pollution further.
39 Compared to the clean daytime on 1 December, the maximums of the boundary layer
40 height (BLH) reduced about 44% and 56% on 2–3 December, when the average $PM_{2.5}$
41 (PM_{10}) concentrations in afternoon hours (from 1200 to 1400 LST) were 44 (48) μg
42 m^{-3} and 150 (120) $\mu\text{g} \text{m}^{-3}$. Part of these reductions of the BLH was also contributed
43 by the effect of the heat storage in the urban canopy.

44

45 **1 Introduction**

46 In recent years, fine particulate matter (PM) pollution events in the atmospheric
47 boundary layer (ABL), i.e., involving particles with diameters $\leq 2.5 \mu\text{m}$ ($PM_{2.5}$), have
48 occurred frequently in urban areas, thus emerging as a serious environmental issue in
49 China. The Beijing-Tianjin-Hebei (BTH) metroplex region is one of the most
50 seriously affected areas in China with respect to air pollution. The main hazards or
51 negative effects of air pollution generally fall into two categories: human health and
52 traffic. Thus, it is an issue that has attracted considerable public attention and,
53 accordingly, numerous studies have focused on investigating the sources and
54 formation mechanisms of air pollution in the BTH region, through numerical

55 simulation and field observational methods (e.g., Wang et al., 2013; Sun et al., 2014;
56 Ye et al., 2016; Li et al., 2017; Han et al., 2018).

57 Beijing, the main city of the BTH region, has experienced several high-impact,
58 persistent, and severe air pollution episodes in recent years, with notable examples
59 having taken place in January 2013, October and November 2014; December 2015
60 and 2016, and January 2017. Beijing is located in the North China Plain (NCP), and is
61 surrounded by the Yan and Taihang Mountains from north to west. Therefore, Beijing
62 is frequently affected by thermally induced mountain-plain wind circulation over the
63 NCP, which contributes to the transportation of air pollution in Beijing (Liu et al.,
64 2009; Hu et al., 2014; Chen et al., 2017; Zheng et al., 2018). In addition, it is well
65 recognized that high levels of anthropogenic emissions and rapid formation of
66 secondary aerosol are key factors leading to the frequent occurrence of severe haze
67 episodes (Li et al., 2017). More importantly, these interactions on local and large
68 scales are associated with the meteorological conditions (Sun et al., 2013; Yang et al.,
69 2018). Previous studies have reported that heavy pollution in Beijing is highly related
70 to unfavorable local weather conditions, such as weak wind, strong temperature
71 inversion, high relative humidity (RH) and low surface pressures (Zhang et al., 2014,
72 Liu et al., 2017, Li et al., 2018).

73 Many studies have also suggested that the structure of the urban boundary layer
74 (UBL), in particular wind, turbulence and stability, had strong influences on the
75 occurrence, maintenance, vertical diffusivity of air pollutants (Han et al., 2009; Zhao
76 et al., 2013). For instance, emissions of air pollution in urban areas lead to a buildup
77 of pollutant concentrations due to reduced mixing and dispersion in UBL (Holmes et
78 al., 2015). An analysis of the dramatic development of a severe air pollution event on
79 November 2014 in the Beijing area revealed that turbulent mixing played an
80 important role in transporting the heavily polluted air and PM_{2.5} oscillations (Li et al.,
81 2018). The vertical profiles of wind and temperature along with the BLH are the main
82 factors affecting turbulence diffusion. Moreover, the BLH is also a key variable in
83 describing the structure of UBL, and in predicting air-pollution (Stull, 1988; Miao et
84 al., 2011; Barlage et al., 2016). Miao et al. (2018) found that the concentration of

85 PM_{2.5} anti-correlates with the BLH. In addition, air pollutants also can modulate
86 radiative transfer processes through the scattering, reflection and absorption of
87 shortwave radiation and reflection, absorption and emission of longwave radiation
88 (Dickerson et al., 1997; Stone et al., 2008; Wang et al., 2014). In response to reduced
89 solar radiation, the cooling of surface air temperature can lead to strong temperature
90 inversion in the near-surface layer, which can increase the atmospheric stability and
91 prolong the accumulation of pollution because of the existence of this stable boundary
92 layer (Barbaro et al., 2013; Che et al., 2014; Gao et al., 2015). A positive feedback
93 loop in which more aerosol loading leads to a more stable atmospheric boundary layer
94 (ABL), enhanced accumulation of pollutants within the ABL, and a more polluted and
95 hazier atmosphere, was described by Zhang et al. (2013; 2018). It is also found that
96 the further worsened meteorological conditions caused by cumulated aerosol pollution
97 subsequently occurred "explosive growth" of PM_{2.5} mass, which often appears in the
98 late stage of heavy aerosol pollution episode in Beijing-Tianjin-Hebei area in China
99 (Zhong et al., 2017).

100 Although many studies have provided various interesting findings, consensus has
101 not been reached on the pollutant transport mechanism and the nature of the
102 interactions between the air pollution and the structure of the UBL, mainly due to a
103 lack of reliable and detailed field measurements and the complex properties of the
104 UBL. Additionally, as mentioned above, there are several factors that affect the
105 occurrence of urban air pollution, which can lead to different pollutant transporting
106 mechanism characteristics for different pollution events. Therefore, taking a severe
107 heavy pollution event occurred during 1–4 December, 2016 in Beijing as an example,
108 we will aim to investigate evolution characteristics of ABL structure and further
109 explore the interaction between the structure of the UBL and the air pollution by using
110 the field data collected from a 325-m meteorology tower in Beijing urban area, as
111 well as from a Doppler wind lidar and a dual-wavelength (1064 and 532 nm)
112 depolarization lidar. During this pollution episode, the PM_{2.5} concentration rapidly
113 increased from about 100 $\mu\text{g m}^{-3}$ to approximately 500 $\mu\text{g m}^{-3}$ at 1200 LST on 4
114 December, which can be considered as a typical case to achieve a better

115 understanding the formation, transportation, and dispersion mechanisms of the alike
116 pollution event, as well as the interactions between the air pollution and the structure
117 of the UBL.

118 The paper is organized as follows: Section 2 describes the field site, data, and
119 methods. The overall characteristics of the synoptic pattern and the meteorological
120 factors related to the development of the pollution event are investigated in Section 3.
121 The impacts of the vertical UBL structure evolution on this pollution episode, and
122 vice versa—especially the turbulence due to the radiative forcing of aerosols—are
123 also explored in Section 3. Lastly, the results of the study are summarized in Section
124 4.

125 **2 Materials**

126 **2.1 Site and data**

127 The main data used in this study were from a tall tower in Beijing, officially known
128 as “the Beijing 325-m meteorological tower” which is located at an urban site in the
129 city (39.97°N, 116.37°E; the Beijing “inner-city” site). Within a radius of 5 km of the
130 tower, buildings of different heights are distributed irregularly in all directions, and
131 the area is surrounded by four-story to twenty-story buildings with heights of 10 – 60
132 m (Liu et al., 2017). The surrounding buildings can be seen in Fig.1a. This tall tower
133 conducts turbulent flux measurements using sonic anemometers (Model Windmaster
134 Pro, Gill, UK) at three different levels (i.e., 47-m, 140-m and 280-m).
135 Note that CSAT3 three-dimensional sonic anemometers designed by Campbell
136 Scientific Inc (USA) at these three levels have been replaced by the Model
137 Windmaster Pro since 2015, so the turbulence measurements before 2015 used in
138 previous papers were collected using the CSAT3 sonic anemometers. The new sonic
139 anemometer experimental setup has been reported by Cheng et al. (2018). Downward-
140 pointing and upward-pointing pyrgeometers and pyranometers (CNR1, Kipp &Zonen)
141 are maintained at the same heights as the sonic anemometers to measure
142 four-component radiation (i.e., incoming shortwave and longwave radiation, and

143 outgoing shortwave and longwave radiation). Meteorological elements, including
144 wind speed, wind direction (010C cup anemometers and 020C wind vanes, Metone,
145 USA), RH and temperature (HC2-S3, Rotronic, Switzerland) are measured at 15
146 levels (i.e., 8-m, 15-m, 32-m, 47-m, 65-m, 80-m, 100-m, 120-m, 140-m, 160-m,
147 180-m, 200-m, 240-m, 280-m and 320-m) above ground level. An Aerodyne aerosol
148 chemical speciation monitor and a high-resolution time-of-flight aerosol mass
149 spectrometer were deployed at 260-m and ground level, repetitively to measure PM₁
150 mass concentrations at 5-min intervals (Sun et al., 2016).

151 In addition, wind speed (05103-L, R. M.Young) and temperature (HMP45C,
152 Vaisala) at the 2.2-m level are measured at a surface station about 20 m south of the
153 tower. We also used wind data collected above 100 m by a Doppler wind lidar
154 (Windcube200, Leosphere, Orsay, France) situated on the rooftop of a 8 m high
155 building. Furthermore, a dual-wavelength (1064, and 532 nm) depolarization lidar
156 developed by the National Institute for Environmental Studies, Japan, sits on the
157 rooftop of a 28 m high building (Yang et al., 2017), which provided us with
158 information on aerosols at higher layer. The mass concentrations of PM_{2.5} measured at
159 the Beijing Olympic Sports Center (Aoti surface station) of the National Air
160 Quality Monitoring Network of China using Tapered Element Oscillating
161 Microbalance analyzers with hourly monitored readings, were obtained from the
162 website of China National Environmental Monitoring Center
163 (<http://113.108.142.147:20035/emcpublish>).

164 The three-dimensional sonic anemometers original records (10 Hz) were
165 processed, prior to analysis using the methods of double rotation (i.e., yaw and pitch
166 rotations) and linear detrending. Wang et al. (2014) tested a few averaging periods and
167 found that a 1-h averaging period is reasonable at this urban site. The processing of
168 turbulence data in our study followed the method described by Wang et al. (2014).

169 The criterion of threshold carrier-to-noise ratio (CNR) was used to reduce the
170 effects of invalid data on profiles derived from the Doppler velocities. The data
171 control process was described in detail by Huang et al. (2017). We calculated the
172 vertical velocity variance and stream wise wind speed and wind direction over a

173 30-minute segment.

174 The dual-wavelength depolarization lidar was used to retrieve the aerosol vertical
175 structure at a spatially resolved resolution of 6 m and temporally resolved resolution
176 of 10 s, but only for altitudes in excess of 100 m because of an incomplete overlap
177 between the telescopic field of view and the laser beam. For this study the raw
178 temporal resolution of the retrieved aerosol profiles was set at 30-minute. More
179 details on the lidar instruments and various data processing techniques were provided
180 by (Yang et al., 2017).

181 The NCEP FNL (Final) Operational Global Analysis data collected every six
182 hours, at 0200, 0800, 1400 and 2000 LST, on $1^\circ \times 1^\circ$ grids were used to analyze the
183 synoptic-scale weather conditions.

184 **2.2 Methods**

185 **2.2.1 Turbulent flux and radiation calculation**

186 The sensible heat and latent heat fluxes were calculated using the
187 eddy-covariance method:

$$188 \quad H = \rho C_p \overline{w'T'} \quad (1)$$

$$189 \quad LE = L_v \overline{w'q'} \quad (2)$$

190 where ρ is the air density (kg m^{-3}), C_p is the specific heat capacity at constant
191 pressure ($\text{J kg}^{-1} \text{K}^{-1}$), w is the vertical velocities (m s^{-1}) from the sonic anemometers,
192 T is the air temperature (K), L_v is the the latent heat of vaporization of water (J kg^{-1}),
193 and q is the specific humidity (kg kg^{-1}). The overbar denotes time averages and an
194 averaging period of 60 minutes was used in this study.

195 The surface energy budget (SEB) without consideration of horizontal advection
196 is usually formulated as

197
$$R_n + Q_F = H + LE + G \quad (3)$$

198 where H is the sensible heat flux from the surface to the adjacent air, LE is the latent
199 heat flux into the atmosphere associated with evapotranspiration, and G is the ground
200 and urban canopy heat storage. R_n is the net radiation, which can be described as

201
$$R_n = DSR - USR + DLR - ULR \quad (4)$$

202 DSR stands for downward shortwave radiation, USR for upwelling short-wave
203 radiation, DLR for downward incoming long-wave radiation, and ULR for
204 upwelling long-wave radiation. The anthropogenic heat flux (Q_F) is a significant term
205 in urban areas, which is the additional energy released by human activities, however
206 its estimation is difficult due to the absence of accurate energy consumption and
207 traffic flow data. In this study, heat storage term minus the anthropogenic heat flux,
208 $G - Q_F = R_n - H - LE$, will be analyzed

209 **2.2.2 Determination of UBL depths**

210 Lidar techniques have become one of the most valuable and popular systems to
211 detect the atmosphere because of their higher spatiotemporal resolution. As a result,
212 many techniques have been developed to determine the BLH by using the remote
213 sensing instruments, such as radar wind profilers, aerosol lidars, and ground-based
214 microwave radiometers (Flamant et al., 1997; Emeis et al., 2004, Haman et al., 2012).
215 Remote sensing is particularly useful in analyzing vertical profiles of turbulence
216 mixing in UBL, and is generally easier to deploy than radiosondes (Georgoulas et al.,
217 2009).

218 Recently, the turbulence method to define the BLH has been proposed by using
219 the Doppler lidar which can obtain three-dimensional wind. The vertical velocity
220 variance σ_w^2 can be used to describe the density of the turbulence, hence the height of
221 the layer in which vertical velocity variance σ_w^2 exceeds a given threshold is
222 considered as the BLH. Previous investigators have given different values of σ_w^2 for
223 different underlying surfaces (Tucker et al., 2009, Pearson et al. 2010). Barlow et al.
224 (2011) defined the mixing height as the height over London, UK up to which $\sigma_w^2 >$

225 0.1 m² s⁻². Here, we select this method of Barlow et al. (2011), because of the similar
226 urban fraction between central Beijing and London.

227 The 30-min vertical velocity standard deviation between lidar is

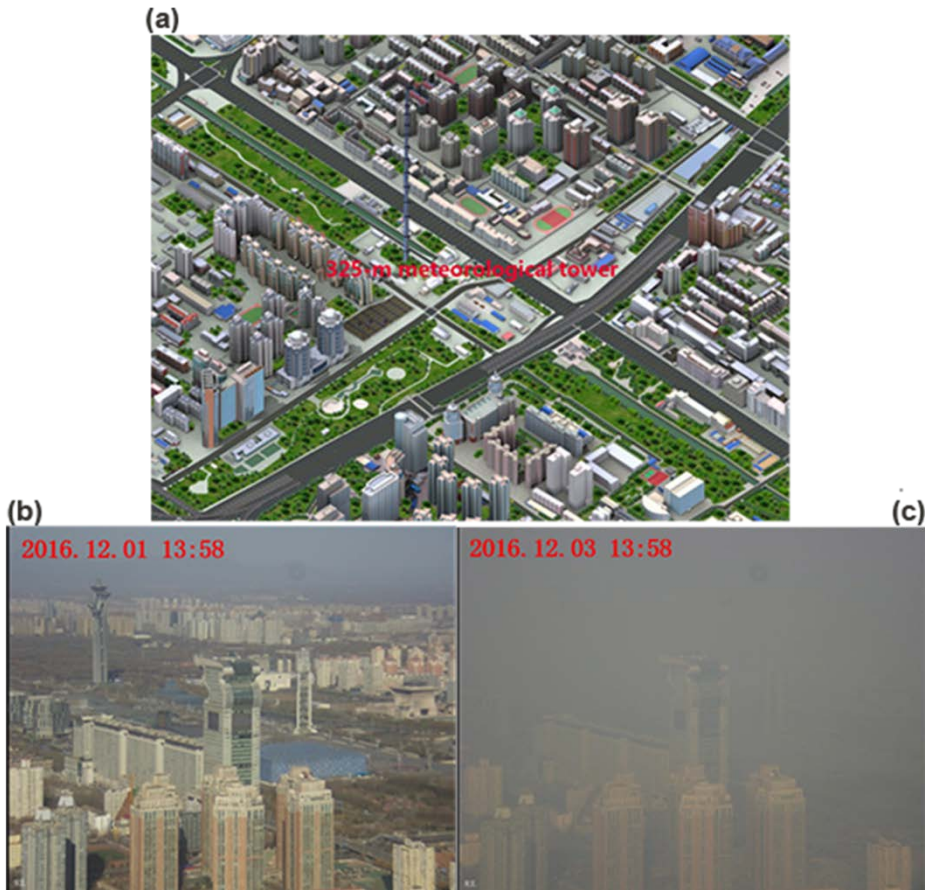
$$228 \quad \sigma_w = \sqrt{\frac{1}{N-1} \sum_{i=1}^N (w_i - \bar{w})^2} \quad (5)$$

229 Where N is the record number every 30 minutes, w_i denotes the i th vertical velocity
230 (m s⁻¹), and \bar{w} is the mean vertical wind speed.

231 **3 Results and discussion**

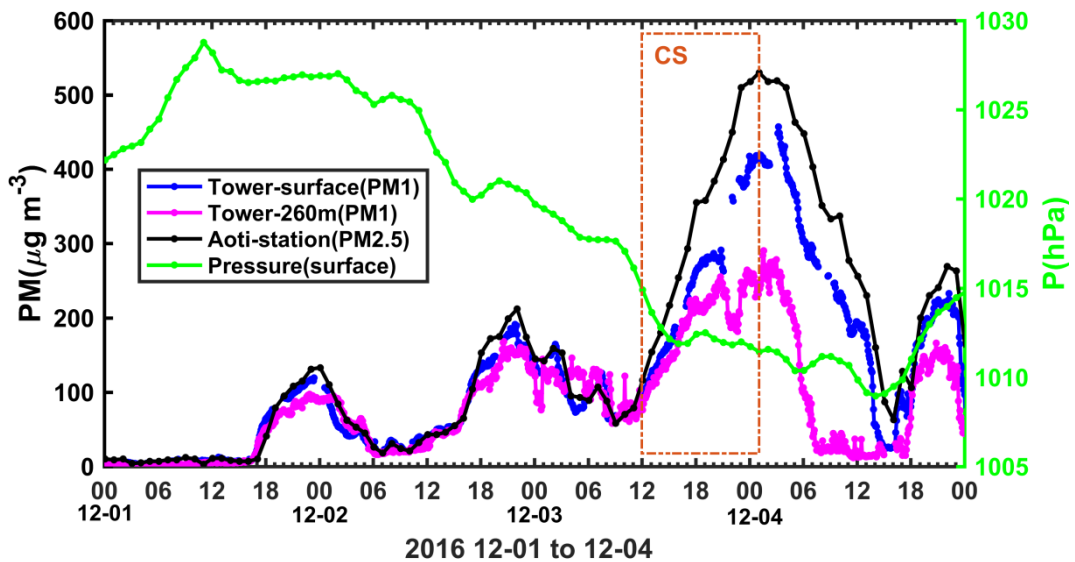
232 **3.1 Air pollution episodes in Beijing**

233 As shown in Fig. 1c, the visibility around the 325-m tower at about 1400 LST on
234 3 December was much lower than that on 1 December. In fact, the visibility decreased
235 rapidly from 1200 to 1600 LST before sunset (1650 LST) on 3 December,
236 accompanied by the increasing PM_{2.5} concentration (from 100 µg m⁻³ to 200 µg m⁻³)
237 at the Olympic Sports Center station and PM₁ concentration (from 100 µg m⁻³ to 190
238 µg m⁻³) at the 325-m tower station (Fig. 2). After sunset, the PM_{2.5} hourly maximum
239 concentration reached 530 µg m⁻³ at 0200 LST 4 December. The cumulative
240 explosive growth process of the pollution, starting at 1200 3 December and lasting till
241 0200 LST 4 December, is defined as cumulative stage (CS).



242

243 **Figure 1: (a) Three-dimensional graph of the underlying surface around the 325-m tower in**
 244 **Beijing. Photographs of the buildings looking north from the 280-m level of the 325-m tower**
 245 **at 1358 LST (b) 1 December and (c) 3 December, 2016.**



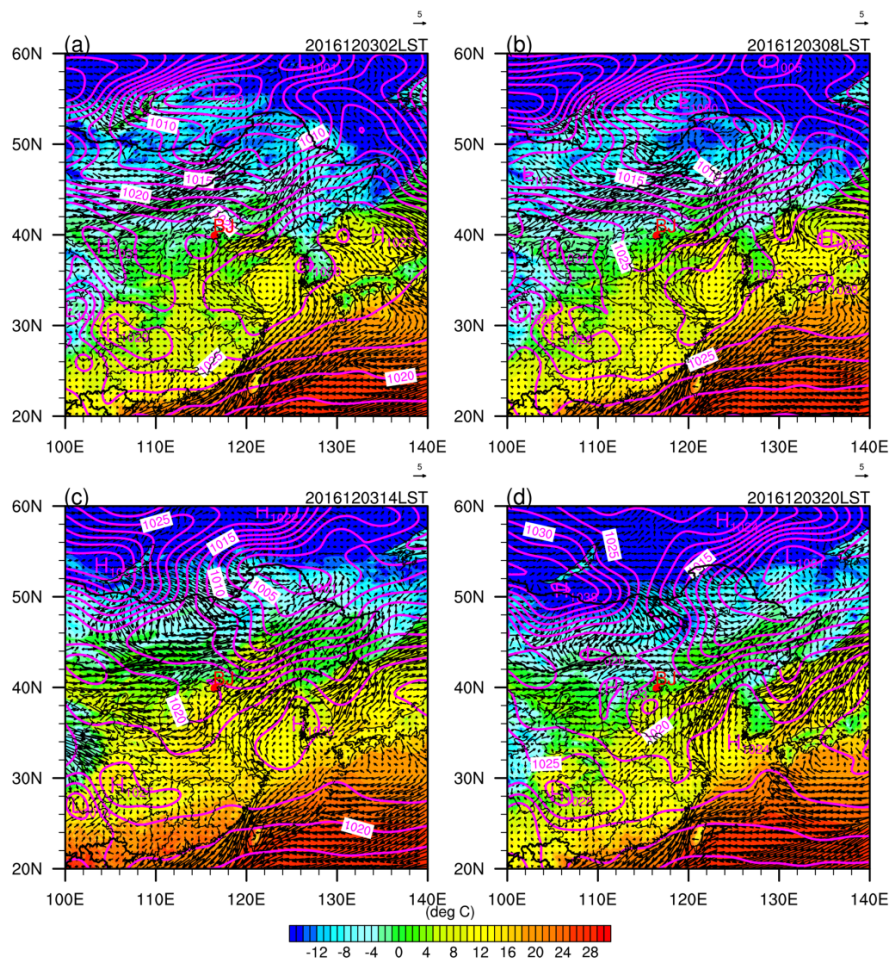
246

247 **Figure 2: Temporal variation of the PM₁ observed at the surface and the 260-m level of the**
 248 **325-m tower, PM_{2.5} at Aoti surface station, and surface pressure at the surface station of the**
 249 **IAP, during 1–4 December 2016. (red box: CS)**

250

The surface pressure measured at the Institute of Atmospheric Physics (IAP)

251 surface station (Fig. 2) indicated the air quality was getting worse with decreasing
 252 surface pressure. In order to analyze the synoptic background fields for the CS, the
 253 sea level pressure and surface wind field on 3 December are shown in Fig. 3. At 0800
 254 LST, the Beijing region was governed by a saddle type pressure field characterized by
 255 uniform pressure, very weak wind speed and changeable wind direction. The surface
 256 high pressure system over the Bohai and Yellow seas was conducive to the
 257 maintenance of these stagnant meteorological conditions till 1400 LST, which
 258 provided the unfavorable meteorological conditions for the diffusion of air pollutants
 259 and contributed to the formation of CS.

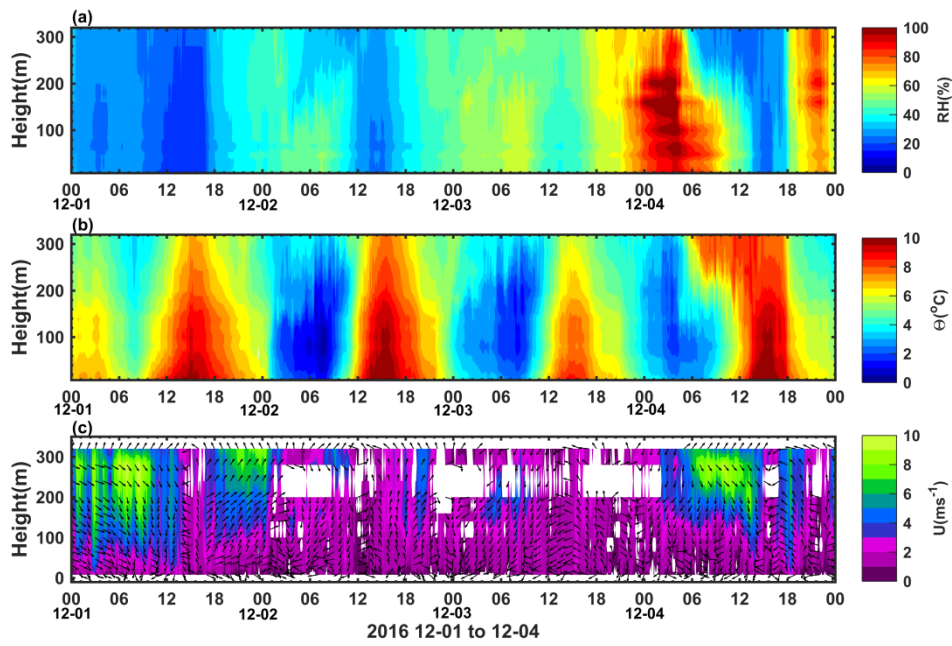


260
 261 **Figure 3: Distribution of surface pressure and temperature at (a) 0200 LST, (b) 0800 LST, (c)**
 262 **1400 LST, and (d) 2000 LST 3 December 2016, where the green star marks the location of**
 263 **Beijing (BJ).**

264 3.2 Meteorological parameters

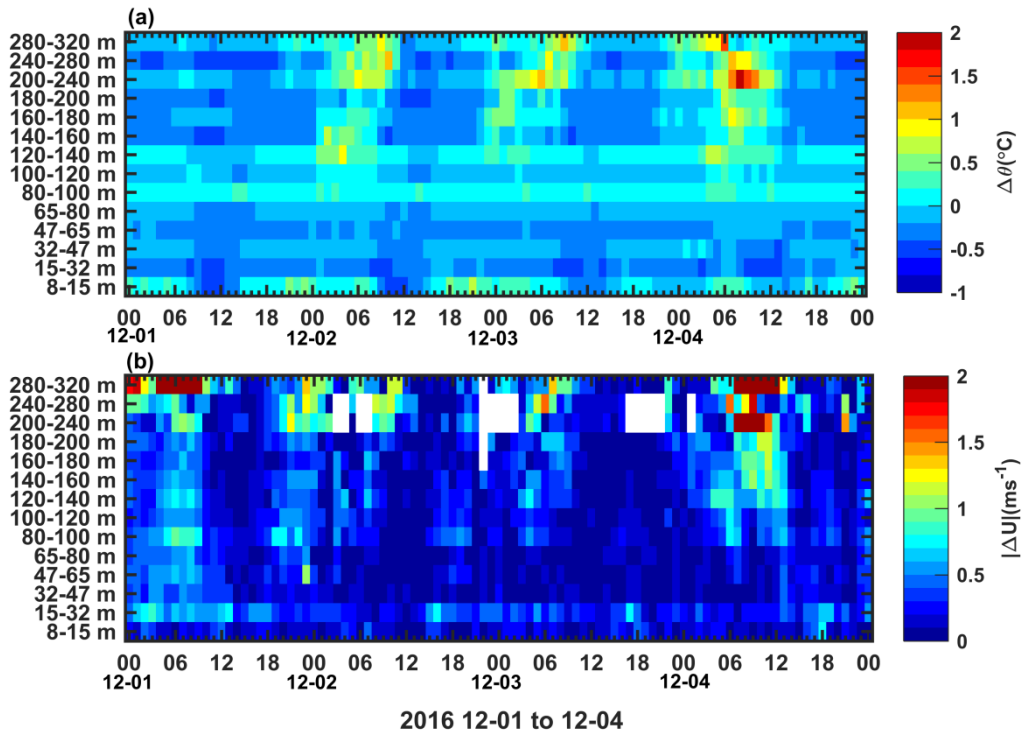
265 As shown in Fig. 4a, RH was mostly larger than 40% during pollution episodes,

266 and increasing along with the concentrated PM_{2.5} (PM₁). Especially during the CS,
267 RH could reach near to 100% at nighttime, which firstly appeared at the levels of
268 160–220 m and then extended to the lower levels. Meanwhile, the deeper RH (>80%)
269 with higher PM concentrations during the CS was possibly caused by secondary
270 aerosol formation. Due to aerosol cooling force, θ at the daytime on 3 December
271 was much lower than on other days. Clearly, the wind flow played an important role
272 in the air pollution process. The southwesterly wind transported air pollutants from
273 Hebei Province to Beijing on the first two pollution nights (Fig. 4c). In order to
274 investigate the characteristics of the UBL structure, the vertical gradients of potential
275 temperature ($\Delta\theta = \theta_2 - \theta_1$) and gradient absolute values in wind speed ($|\Delta U| =$
276 $|U_2 - U_1|$) were calculated by using the adjacent two levels as the thermal and
277 dynamic factors (Fig. 5). It was found that the vertical gradients of wind speed and
278 potential temperature were small because of strong vertical thermal mixing during
279 daytime, whereas they were large at nighttime due to weak vertical mixing.
280 Temperature inversions were found at all three nights, which was negative to the
281 dispersion of the pollutants (Li et al., 2018; Wang et al., 2019). Typically, the
282 formation of temperature inversions in winter night is associated with the radiative
283 cooling effect. Zhong et al. (2019) found that the temperature reduction because of the
284 aerosol cooling force during daytime induced or reinforced an inversion, and then this
285 enhanced inversions further worsen the aerosol pollution. This two way feedback
286 mechanism between unfavorable meteorological conditions and cumulative aerosol
287 pollution also appeared in our case. The values of $\Delta\theta$ and the duration of $\Delta\theta > 0$
288 increased day by day, meaning the thermal stability strengthened with worsening
289 polluted days. Moreover, a long-term existence of temperature inversion near the
290 surface could be found till 1200 LST 4 December, associated with extremely steady
291 stability. This stable surface stratification resulted in the suppressed diffusion of air
292 pollutants at the surface, causing a dissipation lag for PM₁ at the surface compared to
293 the case at the 260-m level (shown in Fig. 2).



294

295 **Figure 4: Vertical evolution of (a) relative humidity, (b) virtual temperature, and (c) wind**
 296 **speed and wind vectors (arrows), observed at 15 levels of the 325-m tower during 1–4**
 297 **December 2016.**



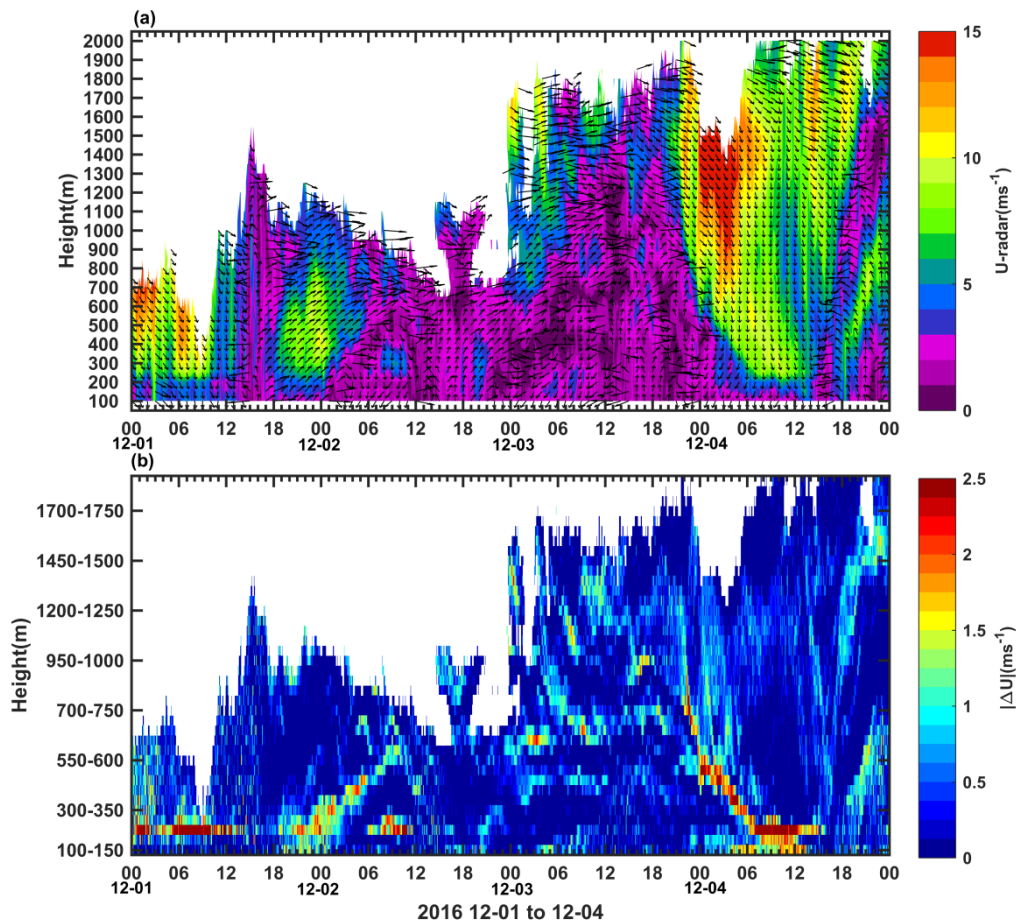
298

299 **Figure 5: Vertical evolution of (a) vertical gradients of relative potential temperature and (b)**
 300 **vertical gradients of zonal wind speed, based on observations at 15 levels of the 325-m tower**
 301 **during 1–4 December 2016.**

302

Owing to the limited height of the tower, the wind profile above several hundred

303 meters collected by the Doppler lidar (Fig. 6) can be used to further investigate the
304 association between the wind flow and air pollution process. On 1 December, the air
305 quality was good before noon and there was strong northwest wind (mostly around 10
306 m s^{-1}) at 200–1000 m levels above the ground (ATG). In our case, notably, a low-level
307 jet (LLJ) established after sunset, with the jet core at 300–500 m ATG, and the
308 maximum wind speed was around 10 m s^{-1} at about 2400 LST. We can see the
309 $\text{PM}_{2.5}/\text{PM}_1$ concentration was starting to increase after sunset with the maximum
310 $\text{PM}_{2.5}$ concentration ($120 \mu\text{g m}^{-3}$) observed at 2400 LST, and then decreased with the
311 gradually weakened LLJ, which suggests this southwesterly LLJ transferred polluted
312 air from the south by advection to Beijing before midnight. A previous study also
313 reported that presence of an LLJ can increase the surface pollution through horizontal
314 advection (Hu et al., 2013). Besides the horizontal advection, LLJ also can generate
315 vertical mixing due to the wind shear with large $|\Delta U| (> 1 \text{ ms}^{-1})$. Once the northern
316 maintain flow generated, the LLJ became weaker ($< 5 \text{ ms}^{-1}$) in the early morning on 2
317 December, and then the vertical mixing generated by the weakened LLJ changed to
318 the dominated term which made an important contribution to the mixing of the
319 pollutants at the dissipated period. Chen et al. (2018) also pointed out that a northerly
320 weak LLJ noticeably reduced the PM concentration in urban Beijing. As a result, the
321 presence of an LLJ has an indispensable effect on the process of the air pollution in
322 the nocturnal boundary layer (NBL).



323

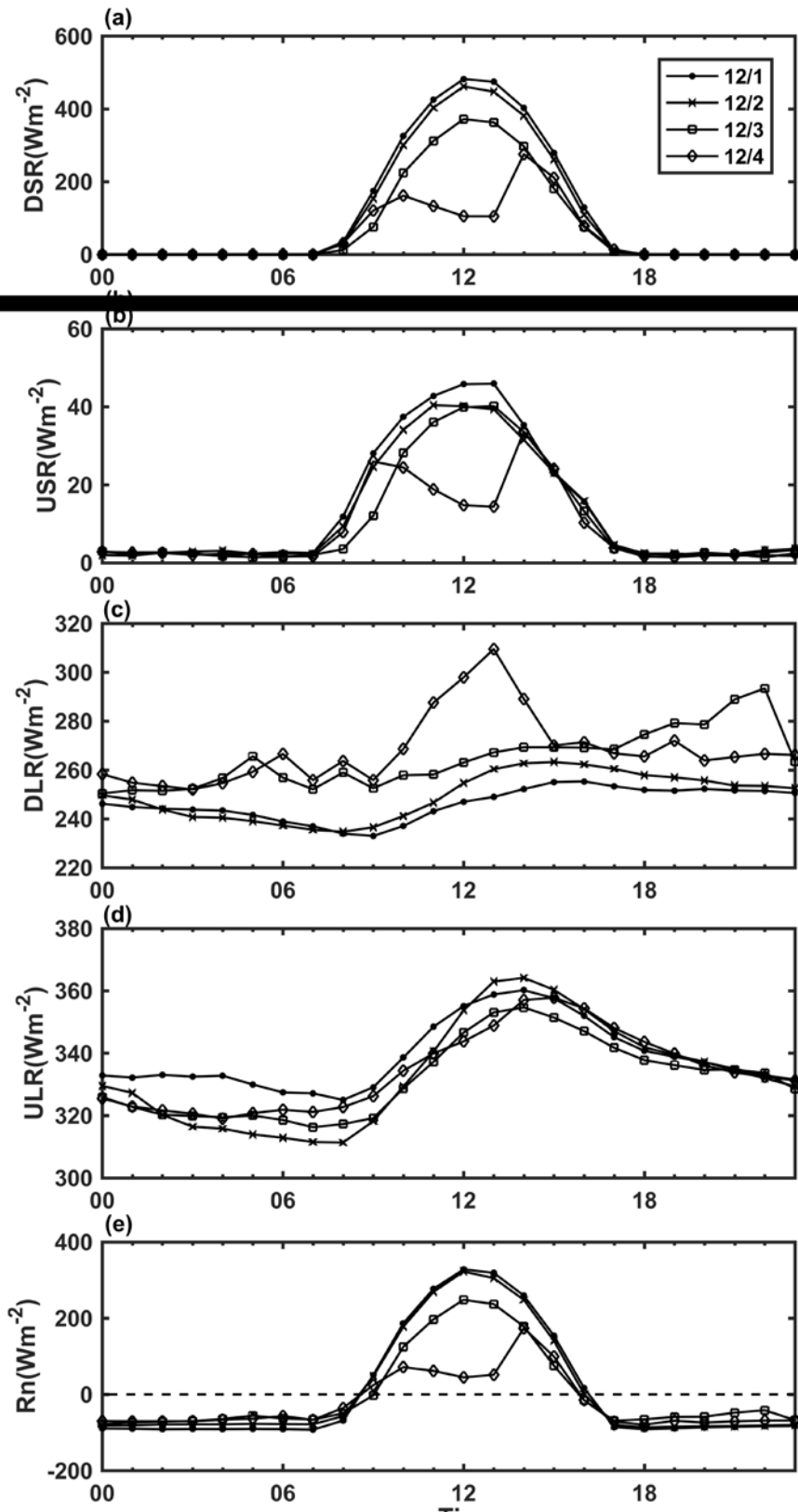
324 **Figure 6: Vertical evolution of (a) wind speed and (b) vertical gradients of wind speed, based**
 325 **on Doppler wind lidar observations during 1–4 December 2016.**

326 We can also see that the PM_{10} concentration at the 260-m level started to
 327 decrease at 0200 LST 2 December which was about two hours later than PM_{10} at the
 328 ground level. This could be explained that the gradually deep and clean northwest
 329 mountain-plain wind occurred first below 100 m ATG, and then reached the upper
 330 level. On 2 December, the wind below 1 km was dominated by speeds of around 2 m
 331 s^{-1} from 0600 to 2200 LST. The weak northerly winds did not fully disperse the air
 332 pollutants before the noon. Meanwhile, after the transition time on 1300 LST,
 333 southerly winds existed and brought polluted air from the south, and then the air
 334 quality became worsened, and the maximum $\text{PM}_{2.5}$ concentration ($210 \mu\text{g m}^{-3}$)
 335 occurred at 2200 LST. Compared to early morning on 2 December, the wind below
 336 600 m was weaker and the vertical gradients (Fig. 6b) were much smaller, meaning
 337 mechanical turbulence (vertical mixing) was extremely weak. Thus, there is no

338 dramatic reduction in the air pollution before sunrise on 3 December, and then the CS
339 began at noon when the wind speeds were mostly lower than 3 m s^{-1} below 1 km ATG,
340 because of the saddle-type pressure-field background (Fig. 3).

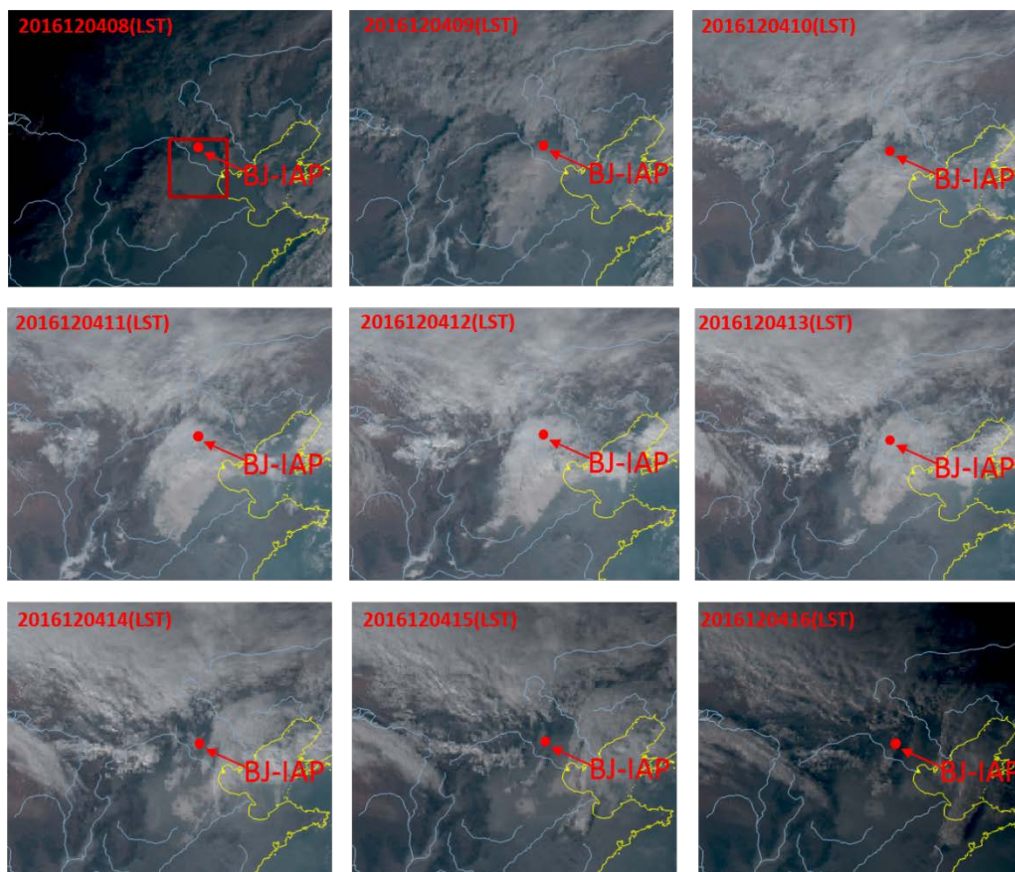
341 **3.3 SEB characteristics**

342 Solar radiation is the most important driver of the development of the UBL.
343 Various climatic changes within urban ABL are driven by the SEB, which distributes
344 the energy by radiation, convection and conduction between a facet (Oke et al., 2017).
345 Therefore, the SEB, described as Eq. 3, is a fundamental aspect contributing to our
346 understanding of the variations in the UBL.



347

348 **Figure 7: Diurnal cycle of (a) downward shortwave radiation, (b) upward shortwave**
 349 **radiation, (c) downward longwave radiation, (d) upward longwave radiation, and (e) net**
 350 **radiation, observed at the 140-m level of the 325-m tower during 1–4 December 2016.**



351

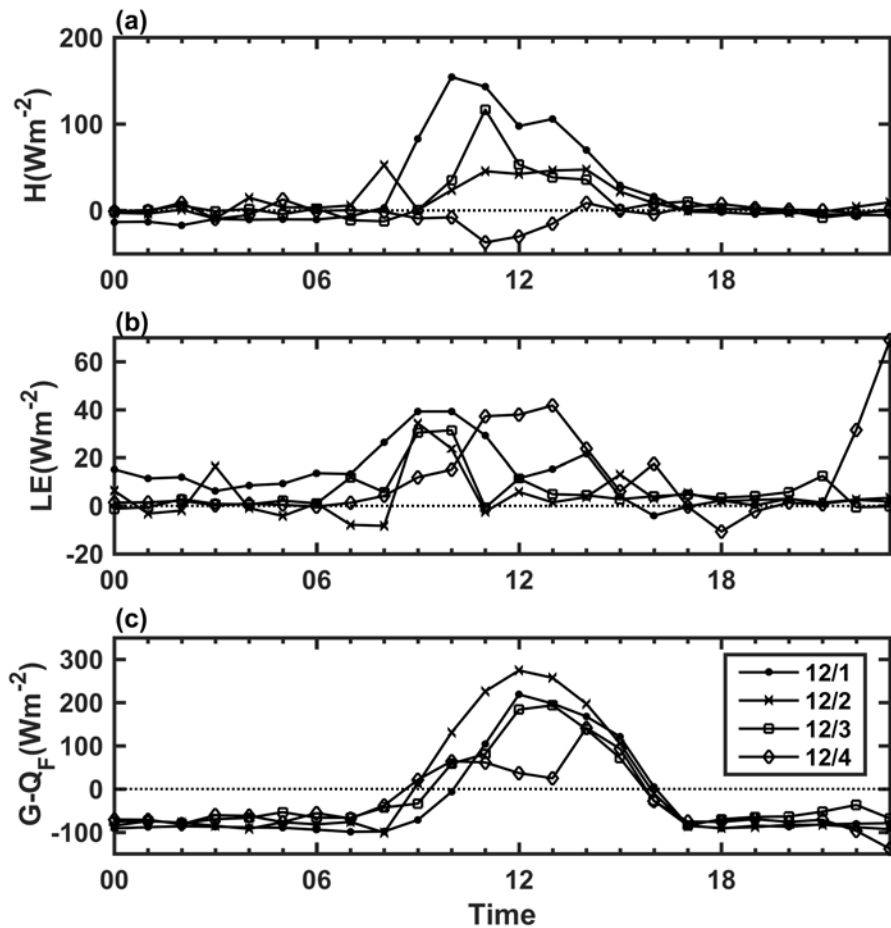
352 **Figure 8: Hourly Himawari-8 geostationary meteorological satellite cloud images from 0800**
 353 **LST to 1600 LST 4 December, where the red point marked the location of IAP station in**
 354 **Beijing, and the red square marked the mass of grey.**

355 In this study, we wanted to focus on the SEB at one level rather than the vertical
 356 difference at between different levels. Moreover, measurements at the 140-m are
 357 above the roughness sublayer layer and are within the surface layer (Miao et al. 2012),
 358 hence only the observations at the 140-m level were used in studying the radiative
 359 exchange. In Fig. 7, the four components shows the daytime pollution received less
 360 shortwave radiation but more longwave radiation than the daytime clean episode. The
 361 *DSR* reduces with gradually worsening air quality on a day-to-day basis. The *DSR*
 362 during this 4-day period reached a peak value (482 W m^{-2}) at 1200 LST 1 December.
 363 The differences between the daytime clean and pollution episodes reached about 20
 364 and 110 W m^{-2} at 1200 LST on 2 and 3 December. On 4 December, the largest
 365 difference was 376 W m^{-2} at 1200 LST, followed by 1400 LST (127 W m^{-2}), which
 366 approximates that at 1400 LST on 3 December (105 W m^{-2}). Overall, compared with
 367 the *DSR* during the daytime clean episode on 1 December, the attenuation ratio of the

368 *DSR* was about 4%, 23% and 78% at 1200 LST 3–4 December, and the averaged
369 value was 5%, 24% and 63% afternoon hours (1200–1400 LST), respectively. Many
370 efforts have been made on the radiative forcing due to the increasing aerosols loading
371 by using model simulations and field experiments (Ramanathan et al., 2001; Xia et al.
372 2007; Ding et al., 2016). Based on observations at the 140-m level at 325-m tower
373 under eight cloudless days (three clean days and five pollution days) in January 2015,
374 Wang et al. (2016) found that the maximum attenuation of the *DSR* was 33.7 W m^{-2}
375 and the attenuation ratio was 7.4% at 1200 LST. Due to the difference in solar angle,
376 degree of pollution, pollutant component, cloud etc., attenuation differences are
377 expected in different case studies. Here, the *USR* on clean days was larger than in
378 pollution days with a larger maximum difference (32 W m^{-2}) on 4 December, which
379 was mainly caused by the lower quantity of *DSR* received on 4 December. For the
380 *DLR*, the diurnal change in the difference between 1 December and 2 December was
381 insignificant. During the other two daytimes, the *DLR* increased with the
382 enhancement of pollution level, and the peak values on 3 December and 4 December
383 were respectively 51 W m^{-2} and 56 W m^{-2} .

384 The diurnal variation of the *DSR* on December 4 was discontinuous, which
385 suggests the large attenuation of the *DSR* on this day was not only the impact of the
386 higher aerosol concentrations, but also that of the cloud cover. The largest *DLR* on 4
387 December also indicated the possibility existence of clouds. Information on the
388 coverage of clouds can be seen from satellite cloud images, which in this case were
389 provided by the products of the Himawari-8 geostationary meteorological satellite,
390 launched by the Japan Meteorological Agency (<http://www.eorc.jaxa.jp/ptree/>).
391 According to these data, the first three days were free from clouds (figures are
392 omitted). From the mass of grey marked by the red square in Fig. 8, it is apparent that
393 pollutants dominated the BTH region at 0800 LST, and then this area became partially
394 cloudy. The area over Beijing was covered with cloud at 1000 LST, which lasted
395 about 3 hours, and then at 1500 LST had become cloudless. Van de Heever and
396 Cotton (2007) found giant nuclei could lead to strong early enhancement of cloud
397 development. Moreover, previous studies have found that cloud fraction changes with

398 aerosol loading (Gunthe et al., 2011; Che et al., 2016). In our case, before the cloudy
 399 day, heavy pollutants occurred over the BTH region, and the IAP station recorded
 400 high relative humidity ($> 90\%$, shown in Fig. 4) at midnight, which would have
 401 enhanced aerosol hygroscopic growth, implying significant aerosol–cloud interactions,
 402 referred to Che et al. (2016). Thus, we can deduce that the cloud cover over the BTH
 403 region may in part account for the aerosols on the pollution days, which supports the
 404 abundant cloud condensation nuclei (CNN) for the cloud formation on the following
 405 day. Certainly, further studies with more measurements data and model simulations
 406 are needed to validate this conclusion.
 407



408
 409 **Figure 9: Diurnal cycle of (a) sensible heat flux, (b) latent heat flux, and (c) heat storage**
 410 **minus anthropogenic heat (termed as $R_n - H - LE$), observed at the 140-m level of the**
 411 **325-m tower during 1–4 December 2016.**

412 In general, the R_n (shown in Fig. 7) attenuation ratio was 3%, 27%, and 68%
 413 respectively, in the afternoon hours, 2–4 December. This attenuation of the radiation

414 in pollution days directly resulted in the change of the SEB. In Fig. 9, clearly, LE was
415 extremely low, at less than 50 W m^{-2} during this 4-day period in winter. The peak
416 value of the H was about 154 W m^{-2} , 53 W m^{-2} , and 117 W m^{-2} , on 1–3 December,
417 respectively. On 3 December, the heat flux showed a dramatically decrease, e.g. from
418 117 W m^{-2} to 53 W m^{-2} in one hour (1100–1200 LST), which aggravated the negative
419 effect on pollutants diffusion (corresponding to the CS). There was a thick
420 temperature inversion near to the surface that lasted till the afternoon on 4 December,
421 as described in last section, which resulted in the downward heat transfer ($H < 0$) to the
422 urban surface in daytime. Gao et al. (2015) also found that large positive radiative
423 forcing reduced the H and LE by $5\text{--}16 \text{ W m}^{-2}$ and $1\text{--}5 \text{ W m}^{-2}$ during a severe fog–
424 haze event over the NCP, by using WRF-Chem model simulations. By analyzing the
425 measurements collected at a rural site (farmland) Gucheng in Hebei Province from 1
426 December 2016 to 31 January 2017 in winter, Liu et al. (2018) confirmed that the
427 mean daily maximum H was only 40 W m^{-2} on heavily polluted days (daily mean
428 $\text{PM}_{2.5}$ concentration $> 150 \mu\text{g m}^{-3}$), but reached 90 W m^{-2} on clean days (daily mean
429 $\text{PM}_{2.5}$ concentration $< 75 \mu\text{g m}^{-3}$). Model simulations have pointed out that the
430 reduced sensible heat resulting from aerosol backscattering could lower the air
431 temperature and suppress the growth of the ABL (Yu et al. 2002). In our case, the
432 large reductions of H on 2–4 December also imply that the high $\text{PM}_{2.5}$ (PM_1)
433 concentrations from the nighttime till after sunrise may have
434 suppressed on the evolution of the UBL. Further and more detailed investigation into
435 the development of the UBL was reported in the next section.

436 Mostly, during daytime, $G - Q_F$ was the largest consuming term in the SEB,
437 accounting for about 65 %, 83 %, 78 % and 71 % averaged in the afternoon hours
438 (1200–1400 LST) on 1–4 December, respectively. Although changes in Q_F at IAP
439 site are unknown due to unavailable accurate energy consumption and traffic flow
440 data, the Q_F term, an additional energy source, is always positive and can be
441 assumed similarly during different days in a short term. Thus, the larger ratio of
442 $G - Q_F$ relative to R_n ($(G - Q_F)/R_n$) implies much more heat is stored in the urban

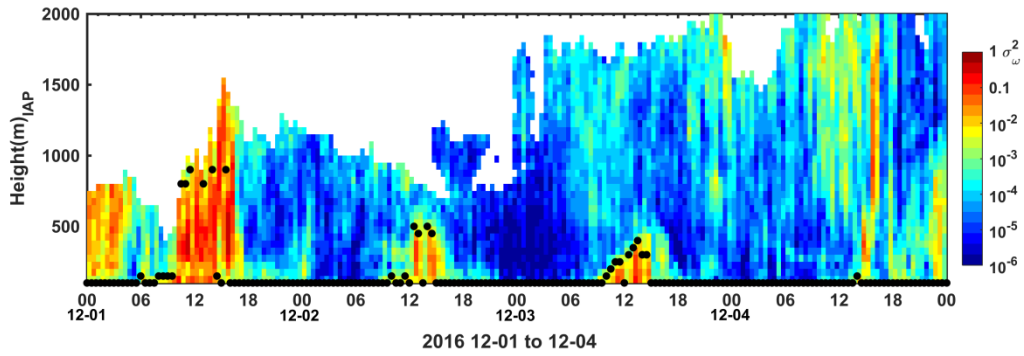
443 canopy, compared with other terms. Heat storage can be affected by different factors
444 including atmospheric conditions (e.g., solar radiation, air temperature and wind
445 speed) and urban characteristics (e.g., urban morphology, material properties and
446 layout configuration) (Meehl and Tebaldi 2004; Lindberg and Grimmond 2011;
447 Miralles et al., 2014; Sun et al., 2017). Urbanization results in land-cover change from
448 vegetative to urban surfaces, and modifies the fractional coverage of urban. The
449 fraction of impervious surfaces around the 325-m tower was investigated using an
450 analytical footprint model and found to exceed 65% (Wang et al., 2015). Such large
451 fraction of impervious urban surfaces in Beijing leads to large urban heat capacity.
452 During the early morning on 2 December, the air temperature near the surface
453 (illustrated in Fig. 4) was lower than on other mornings (i.e., at around 0400 LST,
454 about 5°C lower than on 1 December at 2-m level ABG) and dropped to around zero,
455 meaning a large amount of heat was lost from the urban volume. Then after sunrise,
456 due to the high thermal conductivity of the concrete (about 65 times as large as the
457 air), a considerable part of the R_n (maximum reaching 85% at 1200 LST for $G - Q_F$)
458 was balanced by the heat storage in the urban fabric. Compared with 1 December, the
459 larger heat storage with similar R_n (differing by less than 16 W m^{-2}) on 2 December
460 led to weaker heat flux, which was negative to the diffusion of the pollutants, with a
461 slight increasing trend from 0900 LST to noon, (illustrated in Fig. 2). Specifically,
462 under the conditions of early morning, much more solar heat is absorbed to warm the
463 large urban fabric after sunrise. Besides, previous studies have demonstrated wind
464 was a key determinant of changes in storage heat and the increasing amount of
465 daytime heat storage in urban canopy was strongly tied to lower wind speeds
466 (Grimmond and Oke, 1999; Vautard et al., 2010; Sun et al., 2017). Thus, in this case,
467 the weaker wind (Fig. 4c), associated with weak turbulent transport, contributed the
468 larger heat storage ratios during polluted daytime, in particular on 2 December.
469 Compared with the rural surface, Kotthaus and Grimmond (2014) reported the heat
470 storage in urban surfaces led to delayed warming/cooling after sunrise/sunset, which
471 resulted in the nocturnal stable conditions generally developing later (Barlow et al.,
472 2015). In our study, generally, over the urban surface, compared with the clean

473 daytime, the polluted daytime with calm wind condition not only had reduced R_n and
474 but also larger heat storage ratio, which contributed to weaker heat flux.

475 To improve our understanding of the role of the SEB in air pollution process,
476 more work is needed, such as consideration of the uncertainty in eddy-covariance
477 observations over complex heterogeneous urban surfaces and Q_F . Q_F is a very
478 important term of SEB in urban areas (Sailor 2011, Chow et al., 2014), and this
479 additional heat release will enhance H then increases the air temperature and BLH (Yu
480 et al., 2014). Yang et al. (2018) found that incorporating anthropogenic heat emissions
481 into the modeling system was effective in improving air quality predictions in Beijing.
482 More specific studies in the impacts of the Q_F on the meteorology and air quality of
483 the Greater Beijing area can be made by urban-rural contrast with more observational
484 data, or numerical models in further study.

485 **3.4 Development of the UBL**

486 The diurnal cycle of the ABL exerts strong control on the scalar concentrations
487 of air pollutants (Oke et al., 2017). It is known that the ABL starts to grow after
488 sunrise, and deepens to a maximum value in mid-afternoon, then decreases with the
489 falling off solar radiation reaching at ground surface, during which the whole layer is
490 convectively unstable and well mixed and is defined as CBL. After sunset,
491 accompanied by diminishing turbulence, the boundary-layer depth declines rapidly,
492 and then the boundary layer becomes to the NBL. Based on the general changes in
493 BLH, the TKE at a certain depth or the amount of solar radiation, previous studies
494 have proven that vertical mixing affects pollutants diffusion (Guinot et al., 2006; Sun
495 et al., 2013; Guo et al., 2017). However, few have documented the diurnal circle of
496 the intensity variation of vertical mixing in the UBL, on account of the limitation of
497 instruments. Here, we took advantages of the Doppler lidar (superior spatial and
498 temporal resolution), to quantify the values of the vertical mixing, described as
499 vertical velocity variance σ_w^2 on clean and polluted days.



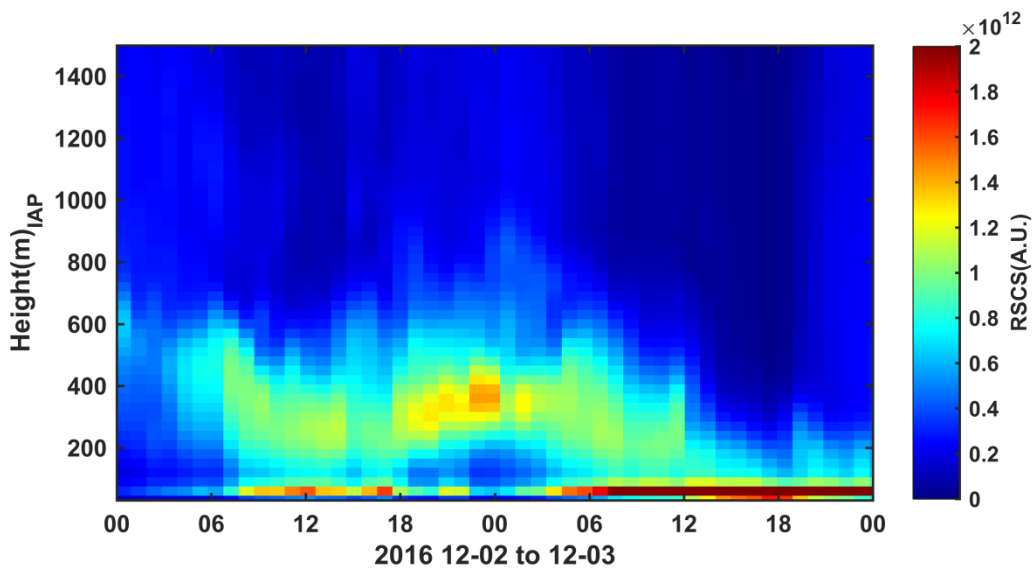
500

501 **Figure 10: Velocity variance, σ_w^2 ($\text{m}^2 \text{s}^{-2}$), calculated from the Doppler wind lidar data.**
 502 **Derived planetary boundary layer depths, based on the threshold method, are depicted as**
 503 **black dots.**

504 As presented in Fig. 10, it was found that the variance of σ_w^2 could characterize
 505 the development of the UBL. σ_w^2 became greater after sunrise (0720 LST), then
 506 reached a maximum at about 1400 LST, exhibiting an obvious trend of decline
 507 (from $\sigma_w^2 > 10^{-1}$ to $\sigma_w^2 < 10^{-2} \text{ m s}^{-1}$) after sunset (1650 LST). When the UBL developed
 508 into NBL, σ_w^2 was about 10^{-3} m s^{-1} at the 200–300 m levels till midnight and
 509 decreased to about 10^{-4} m s^{-1} after midnight until sunset. σ_w^2 was obviously lower
 510 and its vertical distribution shallower during daytime pollution episodes compared
 511 with the daytime clean episode, which is consistent with the results concluded by
 512 analysis of SEB. The diminished R_n and enhanced heat storage ratio during polluted
 513 daytime on 2-4 Dec resulted in the weak vertical mixing. On 4 December, the vertical
 514 mixing was extremely weak, ranging from 10^{-4} to 10^{-5} , and there was barely any
 515 diurnal variation of σ_w^2 till 1500 LST when the $\text{PM}_{2.5}$ (PM_1) had completely
 516 dissipated, which suggests the radiative cooling of aerosols and cloud was a major
 517 factor of influence in the UBL development by suppressing vertical mixing. Weak
 518 turbulence in this stagnating UBL could not broke the deep temperature inversion (Fig.
 519 5a), and such shallow UBL seemed to act an umbrella, blocking the entrainment with
 520 cold-clean air at the upper level, and solar radiation to the surface, and in return,
 521 further suppressing the diffusion of pollutants, leading to not only the increasing
 522 $\text{PM}_{2.5}$ (PM_1) concentration during the CS but also much slower diffusion of PM_1 at
 523 the surface than that at the 260-m level (Fig. 2). Accordingly, in our case study, the

524 two-way feedback mechanism between air pollutants and the UBL is strikingly
 525 responsible for the cumulative and dissipation stage of these pollution episodes.

526 Compared to 1 December, the vertical mixing was weaker till about 5 hours after
 527 the sunrise on 2 December (CS). This weak evolution of the CBL was consistent with
 528 the weak sensible heat flux (Fig. 9). As discussed in Section 3.3, a large amount of the
 529 heat was trapped in the cold urban fabrics under calm wind condition (Fig. 2),
 530 resulting in poor sensible heat flux after sunrise and weak vertical mixing on 2
 531 December.



532
 533 **Figure 11: Evolution of the lidar range-squared-corrected signal (RSCS) at 532 nm from**
 534 **1200 LST 2 December to 1200 LST 3 December 2016. The color scale indicates the intensity**
 535 **of the RSCS, and warm colors represent stronger light scattering.**

536 Additionally, the σ_w^2 was mainly ranged from 10^{-6} to 10^{-5} m s^{-1} ATG to the
 537 detectable observing height during the nighttime from 2200 LST 2 December till the
 538 early morning 0500 LST before the CS on 3 December. This ultra-weak turbulence
 539 transport maintained a very shallow and stable NBL. Note that values of the PM_{10}
 540 concentration (Fig. 2) at the 260-m height of the 325-m tower
 541 changed slightly with the time during the ultra-weak turbulence transport periods.
 542 Moreover, before the CS on 3 December, the aerosol lidar data (Fig. 11) showed that
 543 the gradient of the range-squared-corrected signals (RSCS, calculated by $(RS-RS_0)r^2$,
 544 is applied to compensate for range-related attenuation from the atmosphere, where the
 545 lidar signal RS is corrected for the background noise contribution due to atmospheric

546 skylight and electronic noise of the instrumentation used, the RS_0 is the background
547 signal, and r is the range between the laser source and the target) between the levels of
548 200–250 m and 400–500 m ATG were larger than the other levels from 1800 LST
549 (after sunset) 2 December to 0500 LST (before sunrise) 3 December. As we know,
550 both aerosols and water vapor affect the signals of the lidar. The larger RSCS at the
551 time mentioned above, in our case, must not only have been because of the water
552 vapor but also aerosol concentrations, being consistent with the larger PM_{10}
553 concentration at the 260-m level (more than $100 \mu\text{g m}^{-3}$). Similarly, the larger RSCS
554 between the levels of 200–250 m and 400–500 m ATG illustrated these levels were
555 accumulated with high levels of pollutants and the vertical distribution of pollutants
556 was inhomogeneous, all of which implies that the 260-m level may have been in the
557 residual layer. The pollutants in the residual layer are known to play an important role
558 in the diurnal changes of pollutants at the surface (Hastie et al., 1993; Berkowtiz et al.,
559 2000; Salmond and Mckendary, 2006). Sun et al. (2013) suggested that the high
560 concentration of particles in the residual layer could reach the ground the following
561 morning through convection, causing severe pollutant concentrations in Beijing. In
562 the Tianjin area, Han et al. (2018) also found that a pollution layer was present at the
563 altitude of 1000 m in the early morning on 16 December, 2016, where the aerosols in
564 the higher layers were transmitted to the ground by downward flow before the
565 formation of heavy pollution. Actually, many studies have focused on this mechanism
566 of pollutant vertical mixing in a stable NBL from the micrometeorology perspective.
567 Turbulence in a very stable NBL is typically intermittent and generated by mechanical
568 shear associated with changes in wind velocity with height (Mahrt et al., 1998),
569 referred to as upside-down turbulence in an upside-down boundary structure,
570 compared to the convective daytime case (Mahrt, 1999; Mahrt and Vickers, 2002).
571 This upside-down structure is characterized by TKE (or σ_w^2) and turbulent fluxes
572 increasing with height, and negative transportation of TKE or velocity variances
573 (Banta et al., 2006). As shown in Fig. 10, the σ_w^2 became larger at lower levels from
574 0500 LST 3 December, and then the largest values of σ_w^2 existed at the 500–600 m,
575 along with the corresponding $|\Delta U|$ shown in Fig. 6b. This turbulence could transport

576 the pollutants accumulated in the residual layer downward to the lower levels, and
577 contributed to the later CS of the pollution. Halios and Barlow (2018) also suggested
578 that shear production dominates in the upper half of the UBL, and could therefore not
579 be neglected, even in cases with low wind. Consequently, the intermittent turbulence
580 generated by the wind shear above a stable UBL plays an important role in the vertical
581 spreading of pollutants.

582 As a key variable describing the structure of the UBL, the urban BLH estimated
583 using the threshold method ($\sigma_w^2 > 0.1 \text{ m}^2 \text{ s}^{-2}$) from the Doppler lidar data is also
584 shown in Fig. 10. For the CBL, the diurnal variations of CBL height were not
585 described well by the threshold method for these 4-day, and especially on 4 December
586 for the weak turbulence on polluted day. Eventually, this empirical method was
587 derived using data in autumn or summer, during which the vertical turbulence is much
588 greater than in the winter. In our study, the criterion $\sigma_w^2 > 0.1 \text{ m}^2 \text{ s}^{-2}$ was not
589 applicable because of weak vertical turbulence transport ($\sigma_w^2 < 0.1 \text{ m}^2 \text{ s}^{-2}$) at certain
590 times of the day. The threshold method was also invalid in the NBL during this study
591 period. This may be because of the weak vertical turbulence or smaller height of the
592 NBL falling below the observable height (100 m). Using Windcube100 data during
593 summer in Beijing, Huang et al. (2017) also pointed that this method was reasonable
594 for estimating the CBL depth, while it failed to determine the planetary boundary
595 layer depths for late-night. Subsequently, they defined the NBL top as the height at
596 which the vertical velocity variance decreases to 10 % of its near-surface maximum
597 minus a background variance. However, this new method for the depth of the NBL
598 also failed in our studied period (figure omitted). This is because the NBL in winter is
599 mostly steady, which does not satisfy the near-neutral assumption for the method
600 developed by Huang et al. (2017). Additionally, the NBL has been a major problem
601 for meteorologists for a long time, especially over polluted urban canopies, which
602 make the problem far more complex. Therefore, further investigation of this method
603 should be made in future.

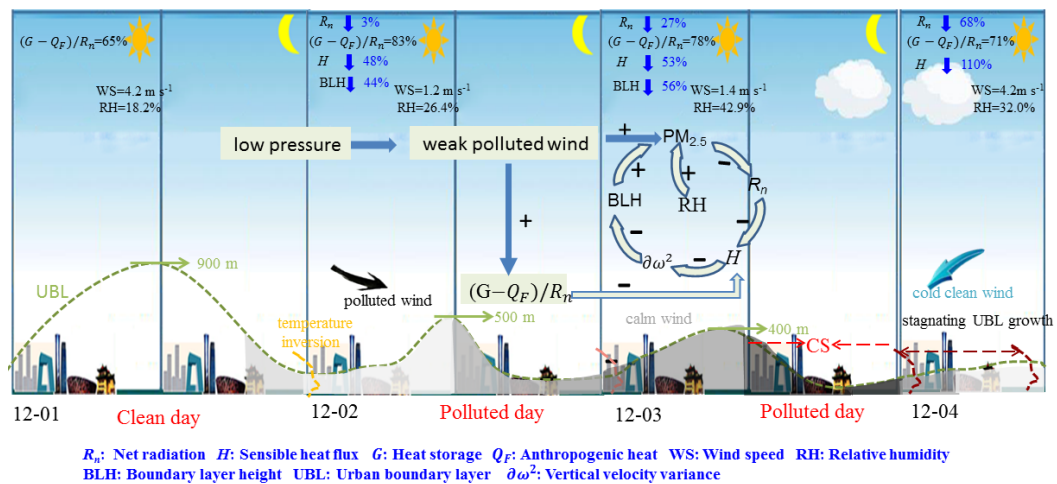
604 Miao et al. (2018) pointed out that the BLH of a fully developed CBL was
605 clearly anti-correlated with the daily $\text{PM}_{2.5}$ concentration, implying that the change in

606 the BLH in the afternoon plays an important role in pollution levels, which is similar
607 with our present. Furthermore, the mixing heights of the fully coupled CBL for 1–4
608 December were about 900 m, 500 m, and 400 m, respectively. Due to the weaker
609 mixing intensity on 4 December, it is difficult to capture specific values of the BLH.
610 As shown in Fig. 2, the maximum daily $PM_{2.5}$ (PM_1) concentrations increased
611 day-by-day from 1 to 3 December, indicating high pollutants concentration near the
612 surface coincide with a shallow CBL. Petäjä et al. (2016) reported that aerosol–
613 boundary layer feedback remained moderate at fine PM concentrations lower than
614 $200 \mu\text{g m}^{-3}$ in Nanjing area, but became intensive at higher PM loadings, and the
615 BLH reduced to half of the original height at particle mass concentrations slightly
616 above $200 \mu\text{g m}^{-3}$. Similarly, particularly strong interactions were verified in the
617 Beijing area when the $PM_{2.5}$ mass concentration was larger than $150\text{--}200 \mu\text{g m}^{-3}$
618 (Luan et al., 2018). In our investigation, the BLH was reduced by about 44% on 2
619 December with the low $PM_{2.5}$ (PM_1) concentration 46 (48) $\mu\text{g m}^{-3}$ and only a 5%
620 attenuation of R_n . Additionally, for the $PM_{2.5}$ (PM_1) concentration of 180 (150) $\mu\text{g m}^{-3}$
621 on 3 December, a 56% reduction of the BLH was found with a 27% attenuation of R_n .
622 Therefore, in addition to the R_n term, it is important to note that the heat storage term
623 in the SEB also makes a significant contribution to the reduction of BLH (details
624 discussed in Section 3.3). Especially, over the megacity Beijing with large fraction of
625 impervious surface, heat storage accounts a great amount of net radiation and its ratio
626 increases with decreasing wind speed, which should be excluded from the quantitative
627 analysis of the impact of aerosol pollutants on UBL. Otherwise, the response degree
628 of the UBL to aerosol pollutants would be overestimated, owing to the polluted days
629 mostly accompanied with weak wind in Beijing.

630 Note that, the BLH reduced significantly from 1 December to 2 December, while
631 the $PM_{2.5}/PM_1$ concentration increased only a little, which implied that the reduced
632 BLH must be a negative factor, yet not the only one, to the dispersion of pollutants.
633 As mentioned in the introduction part, heavy pollution in Beijing is also highly related
634 to high relative humidity (RH), which is positive to the rapid formation of secondary
635 aerosol. On 3 December, during the period, after sunrise before the CS, with weak

636 winds, appreciable near-surface moisture accumulation appeared with RH over 60%
 637 (Fig. 4 c, a), while the RH was about 40% after sunrise on 2 December. Based on the
 638 previous studies (Tie et al., 2017; Zhong et al., 2019), such enhanced moisture on 3
 639 December would reduce direct radiation through accelerating liquid-phase and
 640 heterogeneous reactions to produce more secondary aerosols and enhancing aerosol
 641 hygroscopic growth to increase aerosol particle size and mass (Kuang et al., 2016),
 642 which would back-scatter more solar radiation to space. Thus, the lower RH on 2
 643 December was negative to the formation of secondary aerosol, resulting in the less
 644 $PM_{2.5}/PM_{10}$ on 2 December concentration than on 3 December. Moreover, the
 645 sustained stagnant condition on 2 December contributed to a certain degree of the
 646 $PM_{2.5}/PM_{10}$ concentration before CS, which was one of the preconditions for the rapid
 647 formation of CS.

648 In general, the main impacts of synoptic conditions (pressure, wind, temperature,
 649 relative humidity, etc.), surface energy balance on the UBL evolution, and then the
 650 interactions between the aerosol pollutants and UBL structure can be highly
 651 summarized by a schematic diagram in the present study (Fig. 12), providing a critical
 652 reference for air pollution forecast and assessment in Beijing.



658 **Figure 12: Schematic diagrams of the roles of synoptic conditions, surface energy budget in the development of UBL, and the two-way feedback between UBL structure and accumulation of $PM_{2.5}$ during 1–4 December 2016, the values of meteorological elements averaged in noon hours (1200–1400 LST).**

658 4 Conclusion

659 Using data from the 325-m meteorological tower in Beijing and two nearby

660 lidars, we investigated the characteristics of UBL structure during 1–4 December,
661 2016 in Beijing and examined the interaction between the structure of the UBL and
662 the air pollution during three pollution episodes, especially the rapid CS during which
663 the $\text{PM}_{2.5}$ concentration rose from about $100 \mu\text{g m}^{-3}$ to $500 \mu\text{g m}^{-3}$ in 12 hours. The
664 main conclusions can be summarized as follows.

665 1) During this 4-day study period, the air pollution gradually worsened on a
666 day-by-day basis, with decreasing surface air pressure. Specially, the large-scale
667 circulation with a saddled pressure field was highly unfavorable for the dispersion of
668 pollutants on 3 December during the CS. The RH was larger than 40% during the
669 heavy pollution episodes, and the vertical distribution of RH showed a remarkably
670 inhomogeneous pattern during the peak period of the CS with the deep RH ($> 80\%$) at
671 the 47–240-m levels and heavy surface $\text{PM}_{2.5}/\text{PM}_1$ concentration (about $500 \mu\text{g}$
672 $\text{m}^{-3}/400 \mu\text{g m}^{-3}$) in the early morning on 4 December. Temperature inversion ($\Delta\theta > 0$)
673 occurred during all three nights. For the first pollution episode during the nighttime on
674 1-2 December, a southern neutral LLJ was found at the 200–1000-m levels after
675 sunset till midnight over Beijing, which transported the pollutants from the south of
676 Beijing by advection. For the second episode during nighttime on 2–3 December,
677 weak southerly wind ($< 3 \text{ m s}^{-1}$) dominated below 600-m level, with small vertical
678 gradients, due to the saddle-type pressure-field background. Meanwhile, for CS on 3
679 December, there was a very deep and weak wind layer, which extended to about
680 1100-m level till 2200 LST 3 December, when the accumulated $\text{PM}_{2.5}$ concentration
681 was larger than $400 \mu\text{g m}^{-3}$ at the surface.

682 2) Compared with the *DSR* during the daytime clean episode on 1 December, the
683 attenuation ratio of the *DSR* was about 5%, 24% and 63%, respectively, in the
684 afternoon hours (1200–1400 LST) 2–4 December, which mainly caused a 3%, 27%
685 and 68% reduction of the R_n . The large attenuation of solar radiation on 4 December
686 resulted from the cloud caused by the large aerosol loading with high RH on 3
687 December, possibly supporting plentiful CNN for the formation of cloud. Generally,
688 the latent heat exchange term was very low during these four days over the urban
689 canopy in Beijing, and the dominate term was mostly the heat storage minus

690 anthropogenic heat, calculated as $R_n - H - LE$, during daytime, which accounted
691 for about 65%, 83%, 78% and 71% of R_n (averaged 1200–1400 LST) on 1–4
692 December, respectively. We also found that the lower H appeared on the polluted days
693 than on the clean days, which partly caused by the large consuming term of the heat
694 storage in the urban fabric with calm wind condition.

695 3) In the CBL, the diurnal circle of lidar-based σ_w^2 agreed with the variation of
696 the diurnal cycle of H estimated by the eddy-covariance method at the 140-m level of
697 the 325-m tower, showing that vertical mixing was obviously weakened on polluted
698 days. Compared to the clean day, the evolution of the UBL was delayed by about 5
699 hours after sunrise (about 0720 LST) on 4 December, because of the long-term (> 12
700 hours) existence of temperature inversion resulting from the effects of both aerosols
701 and clouds. This stagnating UBL seemed to act like an umbrella, suppressing the
702 diffusion of PM_{10} at the surface, which was cleaned at about 1500 LST, while the PM_{10}
703 at the 260-m level was driven away by the strong clean northerly wind flow at about
704 0700 LST. Therefore, this two-way feedback mechanism between air pollutants and
705 the UBL was strikingly responsible for the cumulative and dissipation stage of this
706 pollution event in our case. Additionally, the intermittent turbulence generated by the
707 wind shear above the stable NBL in the early morning on 3 December may have
708 contributed to the CS through the downward transporting pollutants from the residual
709 layer. Compared to 1 December the reduction of the maximum BLH was 44% on 2
710 December and 56% on 3 December, whereas, the BLH on 4 December was
711 unobtainable due to the stagnating UBL growth.

712 **Author contributions**

713 LW and GZ determined the goal of this study. LW carried it out, analyzed the
714 data and prepared the paper with contributions from all co-authors. JL, MH and SF
715 helped to process the three-dimensional sonic anemometers, Doppler, and
716 dual-wavelength depolarization lidar original records. SM provided
717 radiation observations. HZ provided Doppler data. YS provided PM_{10} data. TY
718 provided dual-wavelength depolarization lidar data. LW wrote the first manuscript.

719 All authors contributed to the improvement of this manuscript and approved the final
720 version of the paper.

721 **Acknowledgements**

722 This work was funded by the National Key Research and Development Program of
723 the Ministry of Science and Technology of China (2016YFC0203304 and
724 2017YFC0209601) and the open funding of State Key Laboratory of Loess and
725 Quaternary Geology (SKLLQG1842).

726 **References**

- 727 Banta, R. M., Pichugina, Y. L., and Brewer, W. A.: Turbulent velocity-variance
728 profiles in the stable boundary layer generated by a nocturnal low-level Jet, *J. Atmos.*
729 *Sci.*, 63, 2700-2719, 10.1175/JAS3776.1, 2006.
- 730 Barbaro, E., Vilà-Guerau de Arellano, J., Krol, M. C., and Holtslag, A. A. M.: Impacts
731 of aerosol shortwave radiation absorption on the dynamics of an idealized convective
732 atmospheric boundary layer, *Boundary-Layer Meteorol.*, 148, 31-49,
733 10.1007/s10546-013-9800-7, 2013.
- 734 Barlage, M., Miao, S. G., and Chen, F.: Impact of physics parameterizations on
735 high-resolution weather prediction over two Chinese megacities, *J. Geophys. Res.*,
736 121, 10.1002/, 2016.
- 737 Barlow, J. F., Halios, C. H., Lane, S. E., and Wood, C. R.: Observations of urban
738 boundary layer structure during a strong urban heat island event, *Environ. Fluid*
739 *Mech.*, 15, 373-398, 10.1007/s10652-014-9335-6, 2014.
- 740 Berkowitz, C. M., Fast, J. D., and Easter, R. C.: Boundary layer vertical exchange
741 processes and the mass budget of ozone: Observations and model results, *J. Geophys.*
742 *Res.*, 105, 14789-14805, 10.1029/2000jd900026, 2000.
- 743 Bowen, B. M., Baars, J. A., and Stone, G. L.: Nocturnal wind direction shear and its
744 potential impact on pollutant transport, *J. Appl. Meteorol.*, 39, 437-445,
745 10.1175/1520-0450(2000)039<0437:NWDSAI>2.0.CO;2, 2000.
- 746 Che, H. C., Zhang, X. Y., Wang, Y. Q., Zhang, L., Shen, X. J., Zhang, Y. M., Ma, Q. L.,
747 Sun, J. Y., Zhang, Y. W., and Wang, T. T.: Characterization and parameterization of
748 aerosol cloud condensation nuclei activation under different pollution conditions, *Sci.*
749 *Rep.*, 6, 24497, 10.1038/srep24497, 2016.
- 750 Che, H., Xia, X., Zhu, J., Li, Z., Dubovik, O., Holben, B., Goloub, P., Chen, H.,
751 Estelles, V., Cuevas-Agulló, E., Blarel, L., Wang, H., Zhao, H., Zhang, X., Wang, Y.,
752 Sun, J., Tao, R., Zhang, X., and Shi, G.: Column aerosol optical properties and aerosol
753 radiative forcing during a serious haze-fog month over North China Plain in 2013
754 based on ground-based sunphotometer measurements, *Atmos. Chem. Phys.*, 14,
755 2125-2138, 10.5194/acp-14-2125-2014, 2014.
- 756 Chen, Y., An, J. L., Sun, Y. L., Wang, X. Q., Qu, Y., Zhang, J. W., Wang, Z. F., and
757 Duan, J.: Nocturnal low-level winds and their impacts on particulate matter over the
758 Beijing area, *Adv. Atmos. Sci.*, 35, 1455-1468, 10.1007/s00376-018-8022-9, 2018.
- 759 Chen, Y., An, J. L., Wang, X. Q., Sun, Y. L., Wang, Z. F., and Duan, J.: Observation of
760 wind shear during evening transition and an estimation of submicron aerosol
761 concentrations in Beijing using a Doppler wind lidar, *J. Meteor. Res.*, 31, 350-362,

762 10.1007/s13351-017-6036-3, 2017.

763 Cheng, X. L., Liu, X. M., Liu, Y. J., and Hu, F.: Characteristics of CO₂ concentration
764 and flux in the Beijing urban area, *J. Geophys. Res.*, 10.1002/2017jd027409, 2018.

765 Chow W.T. L., Salamanca F. P., Georgescu M., Mahalov A., Milne J. M. and Ruddell
766 B. L.: A multi-method and multi-scale approach for estimating city-wide
767 anthropogenic heat fluxes, *Atmos. Environ.* 99, 64–76,
768 10.1016/j.atmosenv.2014.09.053, 2014.

769 Dickerson, R. R.: The Impact of Aerosols on Solar Ultraviolet Radiation and
770 Photochemical Smog, *Science*, 278, 827-830, 10.1126/science.278.5339.827, 1997.

771 Ding, A. J., Huang, X., Nie, W., Sun, J. N., Kerminen, V. M., Petäjä, T., Su, H., Cheng,
772 Y. F., Yang, X. Q., Wang, M. H., Chi, X. G., Wang, J. P., Virkkula, A., Guo, W. D.,
773 Yuan, J., Wang, S. Y., Zhang, R. J., Wu, Y. F., Song, Y., Zhu, T., Zilitinkevich, S.,
774 Kulmala, M., and Fu, C. B.: Enhanced haze pollution by black carbon in megacities in
775 China, *Geophys. Res. Lett.*, 43, 2873-2879, 10.1002/2016gl067745, 2016.

776 Emeis, S., Münkler, C., Vogt, S., Müller, W. J., and Schäfer, K.: Atmospheric
777 boundary-layer structure from simultaneous SODAR, RASS, and ceilometer
778 measurements, *Atmos. Environ.*, 38, 273-286, 10.1016/j.atmosenv.2003.09.054, 2004.

779 Farrugia, R. N.: The wind shear exponent in a Mediterranean island climate,
780 *Renewable Energy*, 28, 647, 10.1016/S0960-1481(02)00066-6, 2003.

781 Flamant, C., Pelon, J., Flamant, P. H., and Durand, P.: Lidar determination of the
782 entrainment zone thickness at the top of the unstable marine atmospheric boundary
783 layer, *Boundary-Layer Meteorol.*, 83, 247-284, 1997.

784 Gao, Y., Zhang, M., Liu, Z., Wang, L., Wang, P., Xia, X., Tao, M., and Zhu, L.:
785 Modeling the feedback between aerosol and meteorological variables in the
786 atmospheric boundary layer during a severe fog-haze event over the North China
787 Plain, *Atmos. Chem. Phys.*, 15, 4279-4295, 10.5194/acp-15-4279-2015, 2015.

788 Georgoulias, A. K., Papanastasiou, D. K., Melas, D., Amiridis, V., and Alexandri, G.:
789 Statistical analysis of boundary layer heights in a suburban environment, *Meteorol.*
790 *Atmos. Phys.*, 104, 103-111, 10.1007/s00703-009-0021-z, 2009.

791 Grimmond C. S. B. and Oke T. R.: Aerodynamic properties of urban areas derived,
792 from analysis of surface form, *J. Appl. Meteorol.*, 38 1262–92, 10.1175/1520-0450,
793 1999.

794 Guinot, B., Roger, J. C., Cachier, H., Wang, P. C., Bai, J. H., and Yu, T.: Impact of
795 vertical atmospheric structure on Beijing aerosol distribution, *Atmos. Environ.*, 40,
796 5167-5180, 10.1016/j.atmosenv.2006.03.051, 2006.

797 Gunthe, S. S., Rose, D., Su, H., Garland, R. M., Achtert, P., Nowak, A., Wiedensohler,
798 A., Kuwata, M., Takegawa, N., Kondo, Y., Hu, M., Shao, M., Zhu, T., Andreae, M. O.,
799 and Pöschl, U.: Cloud condensation nuclei (CCN) from fresh and aged air pollution in
800 the megacity region of Beijing, *Atmos. Chem. Phys.*, 11, 11023-11039,
801 10.5194/acp-11-11023-2011, 2011.

802 Guo, J. P., Xia, F., Zhang, Y., Liu, H., Li, J., Lou, M. Y., He, J., Yan, Y., Wang, F., Min,
803 M., and Zhai, P. M.: Impact of diurnal variability and meteorological factors on the
804 PM_{2.5} - AOD relationship: Implications for PM_{2.5} remote sensing, *Environ. Pollut.*,
805 221, 94-104, 10.1016/j.envpol.2016.11.043, 2017.

806 Halios, C. H., and Barlow, J. F.: Observations of the morning development of the
807 urban boundary layer over London, UK, taken during the ACTUAL project,
808 *Boundary-Layer Meteorol.*, 166, 395-422, 10.1007/s10546-017-0300-z, 2018.

809 Haman, C. L., Lefer, B., and Morris, G. A.: Seasonal variability in the diurnal
810 evolution of the boundary layer in a near-coastal urban environment, *J. Atmos. Ocean.*
811 *Technol.*, 29, 697-710, 10.1175/jtech-d-11-00114.1, 2012.

812 Han, S. Q., Bian, H., Tie, X. X., Xie, Y. Y., Sun, M. L., and Liu, A. X.: Impact of
813 nocturnal planetary boundary layer on urban air pollutants: measurements from a
814 250-m tower over Tianjin, China, *J. Hazard Mater.*, 162, 264-269,
815 10.1016/j.jhazmat.2008.05.056, 2009.

816 Han, S. Q., Hao, T. Y., Zhang, Y. F., Liu, J. L., Li, P. Y., Cai, Z. Y., Zhang, M., Wang,
817 Q. L., and Zhang, H.: Vertical observation and analysis on rapid formation and
818 evolutionary mechanisms of a prolonged haze episode over central-eastern China, *Sci.*
819 *Total Environ.*, 616-617, 135-146, 10.1016/j.scitotenv.2017.10.278, 2018.

820 Hastie, D. R., Shepson, P. B., Sharma, S., and Schiff, H. I.: The influence of the
821 nocturnal boundary layer on secondary trace species in the atmosphere at Dorset,
822 Ontario, *Atmos. Environ.*, 27A, 533-541, 10.1016/0960-1686(93)90210-P, 1993.

823 Holmes, H. A., Sriramasamudram, J. K., Pardyjak, E. R., and Whiteman, C. D.:
824 Turbulent fluxes and pollutant mixing during wintertime air pollution episodes in
825 complex terrain, *Environ. Sci. Technol.*, 49, 13206-13214, 10.1021/acs.est.5b02616,
826 2015.

827 Hu, X. M., Klein, P. M., Xue, M., Zhang, F. Q., Doughty, D. C., Forkel, R., Joseph, E.,
828 and Fuentes, J. D.: Impact of the vertical mixing induced by low-level jets on
829 boundary layer ozone concentration, *Atmos. Environ.*, 70, 123-130,
830 10.1016/j.atmosenv.2012.12.046, 2013.

831 Hu, X. M., Ma, Z. Q., Lin, W. L., Zhang, H. L., Hu, J. L., Wang, Y., Xu, X. B.,
832 Fuentes, J. D., and Xue, M.: Impact of the Loess Plateau on the atmospheric boundary
833 layer structure and air quality in the North China Plain: a case study, *Sci. Total*
834 *Environ.*, 499, 228-237, 10.1016/j.scitotenv.2014.08.053, 2014.

835 Huang, M., Gao, Z. Q., Miao, S. G., Chen, F., LeMone, M. A., Li, J., Hu, F., and
836 Wang, L. L.: Estimate of boundary-layer depth over Beijing, China, using Doppler
837 Lidar data during SURF-2015, *Boundary-Layer Meteorol.*, 162, 503-522,
838 10.1007/s10546-016-0205-2, 2017.

839 Kotthaus, S., and Grimmond, C. S. B.: Energy exchange in a dense urban
840 environment – Part I: Temporal variability of long-term observations in central
841 London, *Urban Clim.*, 10, 261-280, 10.1016/j.uclim.2013.10.002, 2014.

842 Kuang, Y., Zhao, C.S., Tao, J.C., Bian, Y.X., Ma, N., Impact of aerosol hygroscopic
843 growth on the direct aerosol radiative effect in summer on North China Plain, *Atmos.*
844 *Environ.*, 147(2016), pp. 224-233, 10.1016/j.atmosenv.2016.10.013, 2016.

845 Lee, X. H., Gao, Z. Q., Zhang, C. L., Chen, F., Hu, Y. Q., Jiang, W. M., Liu, S. H., Lu,
846 L. H., Sun, J. L., Wang, J. M., Zeng, Z. H., Zhang, Q., Zhao, M., and Zhou, M. Y.:
847 Priorities for boundary layer meteorology research in China, *Bull. Am. Meteorol. Soc.*,
848 96, ES149-ES151, 10.1175/bams-d-14-00278.1, 2015.

849 Li, J., Sun, J. L., Zhou, M. Y., Cheng, Z. G., Li, Q. C., Cao, X. Y., and Zhang, J. J.:
850 Observational analyses of dramatic developments of a severe air pollution event in the
851 Beijing area, *Atmos. Chem. Phys.*, 18, 3919-3935, 10.5194/acp-18-3919-2018, 2018.

852 Li, X., Zhang, Q., Zhang, Y., Zhang, L., Wang, Y. X., Zhang, Q. Q., Li, M., Zheng, Y.
853 X., Geng, G. N., Wallington, T. J., Han, W. J., Shen, W., and He, K. B.: Attribution of
854 PM_{2.5} exposure in Beijing–Tianjin–Hebei region to emissions: implication to control
855 strategies, *Sci. Bull.*, 62, 957-964, 10.1016/j.scib.2017.06.005, 2017.

856 Li, Z. Q., Guo, J. P., Ding, A. J., Liao, H., Liu, J. J., Sun, Y. L., Wang, T. J., Xue, H.
857 W., Zhang, H. S., and Zhu, B.: Aerosol and boundary-layer interactions and impact on
858 air quality, *Natl. Sci. Rev.*, 4, 810-833, doi:<https://doi.org/10.1093/nsr/nwx117>, 2017.

859 Lindberg F. and Grimmond C. S. B.: The influence of vegetation and building
860 morphology on shadow patterns and mean radiant temperatures in urban areas: model
861 development and evaluation, *Theor. Appl. Climatol.* 105, 311–323,

862 10.1007/s00704-010-0382-8, 2011.

863 Liu, C. W., Gao, Z. Q., Li, Y. B., Gao, C. Y., Su, Z. B., and Zhang, X. Y.: Surface
864 energy budget observed at a winter wheat field site in the north China plain during a
865 fog-haze event, *Boundary-Layer Meteorol.*, 10.1007/s10546-08-0407, 2018.

866 Liu, J. K., Gao, Z. Q., Wang, L. L., Li, Y. B., and Gao, C. Y.: The impact of
867 urbanization on wind speed and surface aerodynamic characteristics in Beijing during
868 1991–2011, *Meteorol. Atmos. Phys.*, 130, 311-324, 10.1007/s00703-017-0519-8,
869 2017.

870 Liu, S. H., Liu, Z. X., Li, J., Wang, Y. C., Ma, Y. J., Sheng, L., Liu, H. P., Liang, F. M.,
871 Xin, G. J., and Wang, J. H.: Numerical simulation for the coupling effect of local
872 atmospheric circulations over the area of Beijing, Tianjin and Hebei Province, *Sci.*
873 *China Ser. D*, 52, 382-392, 10.1007/s11430-009-0030-2, 2009.

874 Luan, T., Guo, X. L., Guo, L. J., and Zhang, T. H.: Quantifying the relationship
875 between PM_{2.5} concentration, visibility and planetary boundary layer height for
876 long-lasting haze and fog-haze mixed events in Beijing, *Atmos. Chem. Phys.*, 18,
877 203-225, 10.5194/acp-18-203-2018, 2018.

878 Mahrt, L., and Vickers, D.: Contrasting vertical structures of nocturnal boundarylayers,
879 *Boundary-Layer Meteorol.*, 105, 351-363, 10.1023/A:1019964720989, 2002.

880 Mahrt, L., Sun, J. I., Blumen, W., Delany, T., and Oncley, S.: Nocturnal
881 boundary-layer regimes, *Boundary-Layer Meteorol.*, 88, 255-278,
882 10.1023/A:1001171313493, 1998.

883 Mahrt, L.: Stratified atmospheric boundary layers, *Boundary-Layer Meteorol.*, 90,
884 375–396, 1999.

885 Meehl G. A. and Tebaldi C.: More intense, more frequent, and longer lasting heat
886 waves in the 21st century, *Science*, 305 994–997, 10.1126/science.1098704, 2004.

887 Miao, S. G., Chen, F., Li, Q. C., and Fan, S. Y.: Impacts of urban processes and
888 urbanization on summer precipitation: A case study of heavy rainfall in Beijing on 1
889 August 2006, *J. Appl. Meteorol. Climatol.*, 50, 806-825, 10.1175/2010jamc2513.1,
890 2011.

891 Miao, S. G., Dou, J. X., Chen, F., Li, J., and Li, A. G.: Analysis of observations on the
892 urban surface energy balance in Beijing. *Sci. China Earth Sci.*, 55(11), 1881-1890,
893 10.1007/s11430-012-4411-6, 2012.

894 Miao, Y. C., Guo, J. P., Liu, S. H., Zhao, C., Li, X. L., Zhang, G., Wei, W., Ma, Y. J.:
895 Impacts of synoptic condition and planetary boundary layer structure on the
896 trans-boundary aerosol transport from Beijing-Tianjin-Hebei region to northeast
897 China. *Atmos. Environ.* 181, 1-11, 10.1016/j.atmosenv.2018.03.005, 2018.

898 Miralles D.G., Teuling A. J., van Heerwaarden C. C. and de Arellano J. V-G.:
899 Mega-heatwave temperatures due to combined soil desiccation and atmospheric heat
900 accumulation, *Nat. Geosci.*, 7, 345–349, 10.1038/NGEO2141, 2014.

901 Oke, T. R., Mills, G., Christen, A., and Voogt, J. A.: *Urban climates*, Cambridge
902 University Press, Cambridge, 157pp, 2017.

903 Pearson, G., Davies, F., and Collier, C.: Remote sensing of the tropical rain forest
904 boundary layer using pulsed Doppler lidar, *Atmos. Chem. Phys.*, 10, 5891-5901,
905 2010.

906 Petäjä, T., Järvi, L., Kerminen, V. M., Ding, A. J., Sun, J. N., Nie, W., Kujansuu, J.,
907 Virkkula, A., Yang, X. Q., Fu, C. B., Zilitinkevich, S., and Kulmala, M.: Enhanced air
908 pollution via aerosol-boundary layer feedback in China, *Sci. Rep.*, 6, 18998,
909 <https://doi.org/10.1038/srep18998>, 2016.

910 Ramanathan, V., Crutzen, P. J., Kiehl, J. T., and Rosenfeld, D.: Aerosols, climate, and
911 the hydrological cycle, *Science*, 294, 2119-2126, 10.1126/science.1064034, 2001.

912 Sailor D. J.: A review of methods for estimating anthropogenic heat and moisture
913 emissions in the urban environment *Int. J. Climatol.* 31, 189–99, 10.1002/joc.2106,
914 2011.

915 Salmond, J. A., and McKendry, I. G.: A review of turbulence in the very stable
916 nocturnal boundary layer and its implications for air quality, *Prog. Phys. Geog.*, 29,
917 171-188, 10.1191/0309133305pp442ra, 2005.

918 Stone, R. S., Anderson, G. P., Shettle, E. P., Andrews, E., Loukachine, K., Dutton, E.
919 G., Schaaf, C., and Roman, M. O.: Radiative impact of boreal smoke in the Arctic:
920 Observed and modeled, *J. Geophys. Res.*, 113, 10.1029/2007jd009657, 2008.

921 Stull, R. B.: *An Introduction to Boundary Layer Meteorology*, Atmospheric Sciences
922 Library, 8, 89 pp., 1988.

923 Sun, T., Kotthaus, S., Li, D., Ward, H.C., Gao, Z., Ni, G.-H., Grimmond, C.S.B.:
924 Attribution and mitigation of heat wave-induced urban heat storage change. *Environ.*
925 *Res. Lett.* 12, 114007, 10.1088/1748-9326/aa922a, 2017.

926 Sun, Y. L., Jiang, Q., Wang, Z. F., Fu, P. Q., Li, J., Yang, T., and Yin, Y.: Investigation
927 of the sources and evolution processes of severe haze pollution in Beijing in January
928 2013, *Journal of Geophysical Research: Atmospheres*, 119, 4380-4398, 10.1002/
929 2014.

930 Sun, Y. L., Wang, Z. F., Wild, O., Xu, W. Q., Chen, C., Fu, P. Q., Du, W., Zhou, L. B.,
931 Zhang, Q., Han, T. T., Wang, Q. Q., Pan, X. L., Zheng, H. T., Li, J., Guo, X. F., Liu, J.
932 G., and Worsnop, D. R.: “APEC Blue”: Secondary aerosol reductions from emission
933 controls in Beijing, *Sci. Rep.*, 6, 20668, 10.1038/srep20668, 2016.

934 Sun, Y., Song, T., Tang, G. Q., and Wang, Y. S.: The vertical distribution of PM_{2.5} and
935 boundary-layer structure during summer haze in Beijing, *Atmos. Environ.*, 74,
936 413-421, 10.1016/j.atmosenv.2013.03.011, 2013.

937 Tie, X., Huang, R.-J., Cao, J., Zhang, Q., Cheng, Y., Su, H., Chang, D., Pöschl, U.,
938 Hoffmann, T., Dusek, U., Li, G., Worsnop, D. R., and O’Dowd, C. D.: Severe
939 Pollution in China Amplified by Atmospheric Moisture, *Sci. Rep.*, 7, 15760,
940 <https://doi.org/10.1038/s41598-017-15909-1>, 2017.

941 Tucker, S. C., Senff, C. J., Weickmann, A. M., Brewer, W. A., Banta, R. M., Sandberg,
942 S. P., Law, D. C., Hardesty, R. M.: Doppler lidar estimation of mixing height using
943 turbulence, shear, and aerosol profiles, *J. Atmos. Ocean. Technol.*, 26(4): 673-688,
944 2009.

945 Van Den Heever, S. C., and Cotton, W. R.: Urban aerosol impacts on downwind
946 convective storms, *J. Appl. Meteorol. Climatol.*, 46, 828-850, 10.1175/jam2492.1,
947 2007.

948 Vautard R., Cattiaux J., Yiou P., Thépaut J-N and Ciais P.: Northern Hemisphere
949 atmospheric stilling partly attributed to an increase in surface roughness *Nat. Geosci.*
950 3, 756–761, 2010.

951 Wang, J. D., Xing, J., Wang, S. X., and Hao, J. M.: The pathway of aerosol direct
952 effects impact on air quality: a case study by using process analysis. In *EGU General*
953 *Assembly Conference Abstracts*, 19, 8568, 2017.

954 Wang, L. L., Li, D., Gao, Z. Q., Sun, T., Guo, X. F., and Bou-Zeid, E.: Turbulent
955 transport of momentum and scalars above an urban canopy, *Boundary-Layer*
956 *Meteorol.*, 150, 485-511, 10.1007/s10546-013-9877-z, 2014.

957 Wang, L. T., Wei, Z., Yang, J., Zhang, Y., Zhang, F. F., Su, J., Meng, C. C., and Zhang,
958 Q.: The 2013 severe haze over southern Hebei, China: model evaluation, source
959 apportionment, and policy implications, *Atmos. Chem. Phys.*, 14, 3151-3173,
960 10.5194/acp-14-3151-2014, 2014.

961 Wang, L., Wang, H., Liu, J., Gao, Z., Yang, Y., Zhang, X., Li, Y. and Huang, M.:

962 Impacts of the near-surface urban boundary layer structure on PM_{2.5} concentrations
963 in Beijing during winter. *Sci Total Environ* 669: 493-504, 10.5194/acp-2018-1184,
964 2018.

965 Wang, X. R., Miao, S. G., Dou, J. X., Dong, P., and Wang, J. L.: Observation and
966 analysis of the air pollution impacts on radiation balance of urban and suburb areas in
967 Beijing, *Chinese J. Geophys.* (in Chinese), 59(11), 3996-4006, 10.6038/cjg20161106,
968 2016.

969 Wang, Y., Li, Z. Q., Zhang, Y., Wang, Q., and Ma, J. Z.: Impact of aerosols on
970 radiation during a heavy haze event in Beijing, *IOP Conf. Ser.: Earth Environ. Sci.*, 17,
971 012012, 10.1088/1755-1315/17/1/012012, 2014.

972 Xia, X. G., Li, Z. Q., Holben, B., Wang, P. C., Eck, T., Chen, H. B., Cribb, M., and
973 Zhao, Y. X.: Aerosol optical properties and radiative effects in the Yangtze Delta
974 region of China, *J. Geophys. Res.*, 112, 10.1029/2007jd008859, 2007.

975 Yang Y.J., Zheng, X.Y., Gao, Z. Q., Wang, H., Wang, T.J., Li, Y.B., Lau, G.I N.C.,
976 Yim,S. H.L.: Long-Term Trends of Persistent Synoptic Circulation Events in
977 Planetary Boundary Layer and Their Relationships with Haze Pollution in Winter
978 Half-Year over Eastern China, *J. Geophys. Res.*,doi: 10.1029/2018JD028982, 2018

979 Yang, T., Gbaguidi, A., Zhang, W., Wang, X. Q., Wang, Z. F. and Yan, P. :
980 Model-Integration of Anthropogenic Heat for Improving Air Quality Forecasts over
981 the Beijing Megacity. *Aerosol Air Qual.Res.*, 18(3), 790-802,
982 10.4209/aaqr.2017.04.0155. 2017.

983 Yang, T., Wang, Z. F., Zhang, W., Gbaguidi, A., Sugimoto, N., Wang, X. Q., Matsui, I.,
984 and Sun, Y. L.: Technical note: Boundary layer height determination from lidar for
985 improving air pollution episode modeling: development of new algorithm and
986 evaluation, *Atmos. Chem. Phys.*, 17, 6215-6225, 10.5194/acp-17-6215-2017, 2017.

987 Ye, X. X., Song, Y., Cai, X. H., and Zhang, H. S.: Study on the synoptic flow patterns
988 and boundary layer process of the severe haze events over the North China Plain in
989 January 2013, *Atmos. Environ.*, 124, 129-145, 10.1016/j.atmosenv.2015.06.011, 2016.

990 Yu, H. B., Liu, S. C., and Dickinson, R. E.: Radiative effects of aerosols on the
991 evolution of the atmospheric boundary layer, *J. Geophys. Res.*, 107,
992 10.1029/2001jd000754, 2002.

993 Yu, M., Carmichael, G.R., Zhu, T. and Cheng, Y. F.: Sensitivity of predicted pollutant
994 levels to anthropogenic heat emissions in Beijing. *Atmos. Environ.*, 89: 169-178,
995 10.1016/j.atmosenv.2014.01.034,2014.

996 Zhang, R. H., Li, Q., and Zhang, R. N.: Meteorological conditions for the persistent
997 severe fog and haze event over eastern China in January 2013, *Science China Earth*
998 *Sciences*, 57, 26-35, 10.1007/s11430-013-4774-3, 2014.

999 Zhang, X. Y., Sun, J. Y., Wang, Y. Q., Li, W. J., Zhang, Q., Wang, W. G., Quan, J. N.,
1000 Cao, G. L., Wang, J. Z., Yang, Y. Q., and Zhang, Y. M.: Factors contributing to haze
1001 and fog in china. *Chin. Sci. Bull.*, 58(13), 1178, doi: 10.1360/972013-150, 2013.

1002 Zhang, X. Y., Zhong, J. T., Wang, J. Z., Wang, Y. Q., and Liu, Y. J.: The interdecadal
1003 worsening of weather conditions affecting aerosol pollution in the Beijing area in
1004 relation to climate warming. *Atmos. Chem. Phys.*, 18, 1-9.
1005 <https://doi.org/10.5194/acp-18-1-2018>, 2018.

1006 Zhao, X. J., Zhao, P. S., Xu, J., Meng, W., Pu, W. W., Dong, F., He, D., and Shi, Q. F.:
1007 Analysis of a winter regional haze event and its formation mechanism in the North
1008 China Plain, *Atmos. Chem. Phys.*, 13, 5685-5696, 10.5194/acp-13-5685-2013, 2013.

1009 Zhong, J. T., Zhang, X. Y., Wang, Y. Q., Sun, J. Y., Zhang, Y. M., Wang, J. Z., Tan, K.
1010 Y., Shen, X. J., Che, H. C., Zhang, L., Zhang, Z. X., Qi, X. F., Zhao, H. R., Ren, S. X.,
1011 and Li, Y.: Relative contributions of boundary-layer meteorological factors to the

1012 explosive growth of PM_{2.5} during the red-alert heavy pollution episodes in Beijing in
1013 December 2016, *J. Meteor. Res.*, 31, 809-819, 10.1007/s13351-017-7088-0, 2017.
1014 Zhong, J. T., Zhang, X. Y., Wang, Y. Q., Wang, J. Z.i, Shen, X. J., Zhang, H. S., Wang,
1015 T. J., Xie, Z. Q., Liu, C., Zhang, H. D., Zhao, T. L., Sun, J. Y., Fan, S. J., Gao, Z. Q.,
1016 Li, Y. B. and Wang, L. L.. The two-way feedback mechanism between unfavorable
1017 meteorological conditions and cumulative aerosol pollution in various haze regions of
1018 China, *Atmos. Chem. Phys.* 19(5): 3287-3306, 10.5194/acp-19-3287-2019, 2019.
1019